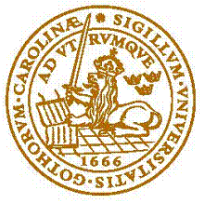

LUND UNIVERSITY

Department of Atomic Physics
Quantum Information Group

Numerical Simulations of Atomic Frequency Comb Quantum Memories for Long Term Storage

Master of Science Thesis

Author:
Fredrik Nilsson
Supervisor:
Lars Rippe

March 12, 2012

Abstract

Quantum memories are used for storing the quantum mechanical states of photons and release identical photons at a later time. This has many applications within the field of quantum computing and is also essential in order to achieve long range quantum communication and cryptography. In this thesis Atomic frequency comb (AFC) quantum memories were investigated. In particular, three-level memory schemes were investigated in detail and a program for simulating these protocols was developed. These schemes make use of control pulses to transfer the population from the optically excited state to a ground state hyperfine level, as well as radio frequency fields to swap the population in the two ground state hyperfine levels. In this work control and RF pulses, tailored to give good transfer rates, are suggested and effects due to off resonant excitation was investigated. A memory protocol which could give efficiencies up to 60% for Pr^{3+}:Y_2SiO_5 based AFC memories is proposed. The main bottleneck for reaching higher efficiencies is that the AFC peak spacing needs to be small in order to give enough time to transfer the population to the spin state with the control pulses. With the control pulses suggested in this work and the current technology of tailoring AFC peaks in Pr-based memories, this gives a maximum finesse of 6 of the AFC structure.

Contents

Chapter 1

Populärvetenskaplig sammanfattning

I den mikroskopiska världen gäller inte samma naturlagar som de vi är vana vid att uppleva när vi undersöker den 'vanliga' makroskopiska världen. Istället för Newtons lagar, som som man lär sig i grundskolan, beskrivs den mikroskopiska världen av kvantmekaniken (Newtons lagar är ett gränsfall av kvantmekaniken). I detta arbete studerade jag så kallade optiska kvantminnen.

Precis som man i en vanlig dator har minnen som lagrar klassisk information, kan man med hjälp av kvantminnen lagra kvantmekanisk information, dvs. kvantmekaniska tillstånd. Optiska kvantminnen används för att lagra kvantmekaniska tillstånd hos ljus. I en vanlig dator så lagras informationen i ettor och nollor, s.k. 'bitar'. En bit i minnet kan antingen ha värdet 1 eller 0. Ett kvantmekaniskt tillstånd behöver inte antingen vara 1 eller 0, utan kan vara i en superposition mellan 1 och 0. Detta gör att man kan konstruera vissa algoritmer som är mycket snabbare än motsvarande algoritmer på en vanlig dator.

En annan applikation där kvantminnen är viktiga är om man vill skicka kvantinformation långa sträckor, detta kallas kvantkommunikation. Kvantkommunikation kan användas i olika krypteringsscheman. 2004 utfördes faktiskt en banktransaktion i Wien som krypterades med hjälp av kvantkryptering.

De kvantminnen jag studerade bygger på att man i en kristall av Yttrium Silikat lagt in små mängder av en sällsynt jordarts metall, Praseodym. Genom att modifiera för vilka frekvenser som Pr-jonerna absorberar ljus så kan man få jonerna att spara tillståndet av en ljuspuls och sedan skicka iväg en identisk ljuspuls efter en viss tid. Jag har utvecklat ett datorprogram för att simulera dessa processer och använt det för att undersöka och optimera Pr-baserade optiska kvantminnen.

Chapter 2

Introduction

In this thesis Atomic Frequency Comb (AFC) Quantum Memories were investigated. AFC memories are optical quantum memories, i.e. they are used to store the quantum mechanical states of photons in order to release identical photons at a later time. This has many interesting aspects and applications. Except for the fact that it is really fascinating in itself to be able to store and control the state of photons, optical quantum memories are essential in order to achieve long-range quantum communication as well as in constructing quantum computers.

Quantum communication, i.e. the transfer of quantum information between distant parties, is a crucial ingredient in all forms of quantum cryptography. Recent developments in the field of quantum computation and quantum cryptography give rise to intriguing possibilities of small quantum networks where quantum information can be stored and manipulated locally and then sent over vast distances.

Just as information is stored in bits (zeros and ones) in a regular computer, quantum information is stored in qubits. The difference between a bit and a qubit is that a qubit is not restricted to the value zero or one, instead any superposition state between zero and one can be used. This allows for construction of specific algorithms that runs faster than the corresponding algorithms for a classical computer. A famous quantum algorithm that made the concept of quantum computation widely known is the factorization algorithm written by Peter Shor 1994.[1]

Sending qubits between distant parties can at first sight seem rather unproblematic. One could imagine a qubit being represented by a polarization state or phase of a photon which then could be transmitted over large distances using optical cables. Indeed there is quantum cryptography equipment which can be used together with the standard telecommunications net available on the market.

However, there are no perfect channels for sending information. In the case of optical cables the probability for photon absorption and photon depolarization both increase exponentially with the length of the cable. Thus the maximum length between two nodes is limited by the absorption length of the cable, which typically is of the order of 100 km (see e.g. [2, 3, 4]). So, Quantum Cryptography and Quantum Key Distribution

(QKD) is already possible to use for encryption in local area networks, for example within financial districts, but fails for larger distances.[1].

In classical communication the problem of attenuation is handled by making use of repeaters at certain nodes in the channels. However, as shown by Wooters and Zurek, quantum signals can neither be cloned nor amplified (see ref. [6]) and thus regular classical repeaters cannot be used for amplifying inheritable quantum mechanical signals. Instead one has to use complex schemes of entanglement swapping and entanglement purification to swap the entanglement between two close by parties to two distant parties. These schemes require the flying photon qubits to be stored locally as stationary quibits and thus some forms of optical quantum memories. [7]

The first optical quantum memory based on an atomic frequency comb was suggested by Afzelius et. al. [8][2] and realised experimentally by Riedmatten et. al. 2008 [9]. Sabooni et. al. have achieved efficiencies of 35% 2010. [10]

The AFC-memory is based on rare-earth-ion-doped-crystals and makes use of the inhomogeneous broadening of the energy levels in the rare-earth-ions to tailor an absorption profile with a comb-like structure. In this thesis a program for simulating three level optical quantum memories was developed and used to investigate Pr^{3+}-doped Y_2SiO_5 AFC memories.

2.1 Level structure of Pr^{3+}:Y_2SiO_5

In this work Pr doped Yttrium Silicate based AFC memories were simulated. The optical transition used for the memory process was $^3H_4 \rightarrow {}^1D_2$. In figure 2.1 the hyperfine structure for this transition is given. In the text the $^3H_4$ 5/2 level will be called the aux-level, $|aux\rangle$, the 3/2-level will be called the ground level, $|g\rangle$, or level 1, the 1/2 level will be called the spin level, $|s\rangle$, or level 2 and the $^1D_2$ 3/2 level will be called the excited level, $|e\rangle$, or level 3.

AFC memories have previously been simulated by solving the two-level Maxwell Bloch equations [11]. Then only the energy levels $|g\rangle$ and $|e\rangle$ have been considered. However, for more complex memory schemes, e.g. those needed for quantum key distribution, the spin level will also be used in the storage process. For this reason a full three-level simulator was developed in this thesis.

2.2 Structure of the Thesis

I will start to discuss the density operator formalism of quantum mechanics since a general understanding of this formalism is required to understand the derivations given in chapter 4. In chapter 5 I discuss and present the theory of the AFC-memory. The

[1]The first banking transaction which used quantum cryptation was made in Vienna 2004 by Zeilinger et. al.[5]

[2]The preprint was published electronically 2008.

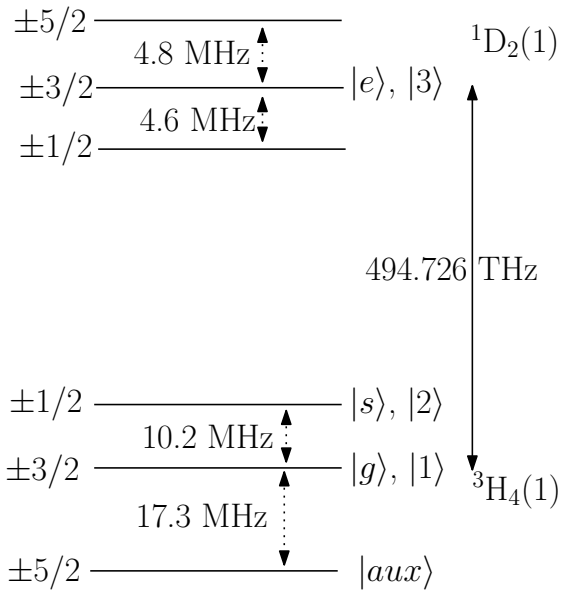

Figure 2.1: Energy level structure of Pr^{3+}:Y_2SiO_5. In the text the 5/2 level will be called the aux-level, the 3/2-level will be called the ground level or level 1, the 1/2 level will be called the spin level or level 2 and the 3/2 level will be called the excited level or level 3.

method and results are presented in chapter 6 and in the last chapter I summarize the work and present the conclusions.

Chapter 3

Density operator formulation of quantum mechanics

Instead of describing the state of a system using quantum state vectors quantum mechanics can be reformulated by making use of the so called density operator. The density operator formulation of quantum mechanics is particularly useful when it comes to describing statistical mixtures of states, or rather ensembles of quantum systems where the total, exact state for the entire ensemble is not known. The density operator of a system is defined as

$$\rho = \sum_i p_i |\psi_i\rangle\langle\psi_i|. \tag{3.1}$$

Here p_i is the probability of obtaining the state $|\psi_i\rangle$ when measuring the state of the ensemble. For a given basis, $\{|a_i\rangle\}$, the density operator can be represented by a matrix whose elements are given by

$$\rho_{ij} = \sum_k p_k \langle a_i|\psi_k\rangle\langle\psi_k|a_j\rangle. \tag{3.2}$$

From this definition it is evident that the trace of the density matrix has to be 1 in order to conserve the total probability.[12, p.98-108], [13, p.174-187], [14]

3.1 Pure and Mixed ensembles

From the definition above it may not be completely evident why the density operator is a useful concept. However, say that you have a statistical ensemble of spin 1/2 particles where half of the particles are in a spin up state along the z-axis and the other half in spin down state along the same axis. One would at first be tempted to describe the state of the spin 1/2 systems as a superposition state between up and down. However, this would mean that that all particles have aligned spins in a certain direction in space, which clearly was not the case for the particular ensemble we were studying. There is actually no way of quantitatively describing this ensemble of atoms using the regular

formulation of quantum mechanics. It is on the other hand very easy to define the density operator for the system as

$$\rho = \frac{1}{2}|+\rangle\langle+| + \frac{1}{2}|-\rangle\langle-|.$$

One could also think of an ensemble of spin 1/2 particles where one third is in a spin up state along the z-axis, one third in a spin down state along the z-axis and one third in a spin up state along the x-axis (corresponding to a superposition between spin up and down along the z-axis). The density matrix for this system is given by

$$\rho = \frac{1}{3}|+_z\rangle\langle+_z| + \frac{1}{3}|-_z\rangle\langle-_z| + \frac{1}{3}|+_x\rangle\langle+_x|.$$

Thus the states in the sum 3.1 do not have to be orthogonal and the number of terms in the sum can exceed the dimension of the ket-space.

If all particles in the ensemble are in the same state, $|\phi\rangle$, the density matrix can be written as $\rho = |\phi\rangle\langle\phi|$. Such a density matrix is said to represent a pure ensemble. However, if all particles are not in the same state the density operator cannot be written on this form. A density operator that cannot be written as $\rho = |\phi\rangle\langle\phi|$ for some state $|\phi\rangle$ is said to represent a mixed ensemble. In the literature pure and mixed ensembles are often referred to as pure and mixed states. This can often lead to confusion since a state mainly refers to a system described by a single state ket, and therefore the nomenclature of ref. [13], with pure and mixed ensembles will be used in this work. From the definition of a pure ensemble it is evident that the density operator for a pure ensemble fulfils the condition $\rho^2 = \rho$. A mixed ensemble is represented by a density matrix that fulfils the condition $Tr(\rho^2) < 1$. [13, p.174-187]

3.2 Quantum measurements in the density operator picture

Measurements on a quantum system described by the state ket $|\psi_i\rangle$ are described by the measurement operator M_m. The probability to measure the eigenvalue m is given by

$$P_{m,i} = \langle\psi_i|M_m^\dagger M_m|\psi_i\rangle = tr(M_m^\dagger M_m|\psi_i\rangle\langle\psi_i|) \tag{3.3}$$

The right hand side of relation 3.4 is just the trace of the absolute square of the measurement operator times the density operator for a pure ensemble. It is straight forward to generalize the expression for an ensemble described by a general density matrix $\rho = \sum_i p_i|\psi_i\rangle\langle\psi_i|$.

$$P_m = \sum_i P_{m,i}p_i = \sum_i p_i tr(M_m^\dagger M_m|\psi_i\rangle\langle\psi_i|) = tr(M_m^\dagger M_m\rho) \tag{3.4}$$

From a similar argument one finds that the density matrix of the ensemble is given by

$$\rho_m = \frac{M_m\rho M_m^\dagger}{tr(M_m^\dagger M_m\rho)} \tag{3.5}$$

after the measurement. [12, p.98-108]

3.3 Time evolution of the density operator

The time evolution of the density operator can be derived from the time evolution of the state kets governed by the Schrödinger equation. Assume that the density operator at some time t_0 is given by $\rho(t_0) = \sum_i p_i|\psi_i, t_0\rangle\langle\psi_i, t_0|$. The Schrödinger equation of the state kets then gives that

$$i\hbar\frac{\partial\rho}{\partial t} = \sum_i p_i \left(H|\psi_i, t_0; t\rangle\langle\psi_i, t_0; t| - |\psi_i, t_0; t\rangle\langle\psi_i, t_0; t|H\right) = -[\rho, H] \tag{3.6}$$

[13, p.174-187]

3.4 Postulates of Quantum Mechanics in the density operator picture

The discussion in the last sections lead up to the following four postulates of quantum mechanics in the density operator picture: [12, p.98-108]

1. Any isolated system has an associated Hilbert space called the state space of the system. The system is completely described by the density operator of the system. If the system is in state ρ_i with probability p_i the density operator is given by

$$\sum_i p_i\rho_i \tag{3.7}$$

   The density operator is positive and has trace 1.

2. The time dependence of the density operator is given by a unitary transformation U so that

$$\rho(t) = U\rho(t_0)U^\dagger \tag{3.8}$$

3. Quantum mechanical measurement are described by a set of operators M_m, called measurement operators. m are the possible outcomes of the measurements. The probability of obtaining the outcome m is given by

$$P_m = tr(M_m^\dagger M_m\rho) \tag{3.9}$$

   and the state after the measurement is described by the density matrix

$$\rho_m = \frac{M_m\rho M_m^\dagger}{tr(M_m^\dagger M_m\rho)} \tag{3.10}$$

4. Consider n individual quantum mechanical systems. The state space of the total system is then the tensor product of the state space of the n individual systems and is described by the density matrix $\rho = \rho_1 \otimes \rho_2 ... \otimes \rho_n$.

Chapter 4

Theory of light matter interaction - Derivations of necessary equations

4.1 Derivation of the Bloch equations for a 3-level system

The following derivation is a generalization of the derivations in refs. [11, 15]

4.1.1 Initial definitions

In this thesis the interaction of 3-level systems with electric and magnetic fields is studied. For transitions between the upper level and any of the two lower lying levels the electric dipole approximation will be made. The two lower lying levels (level 1 and 2 in figure 4.1) are two hyperfine levels with the same quantum number J and thus electric dipole transitions between these levels are forbidden.The dominating transitions between these two levels will therefore be magnetic dipole transitions. Treating the interaction between the atom and the field as perturbations the Hamiltonian is given by

$$H = H_0 + V_{ED} + V_{MD} \tag{4.1}$$

where H_0 is the unperturbed Hamiltonian and V_{ED} is the perturbation with the electric dipole fields and V_{MD} the interaction with the radio frequency magnetic dipole field. The system we are studying is shown in figure 4.1.

The basis states are eigenstates of the unperturbed Hamiltonian

$$H_0|i\rangle = \hbar\omega_i|i\rangle \tag{4.2}$$

where i= 1,2,3.

In this basis H_0 has the form

$$H_0 = \begin{pmatrix} \hbar\omega_1 & 0 & 0 \\ 0 & \hbar\omega_2 & 0 \\ 0 & 0 & \hbar\omega_3 \end{pmatrix}$$

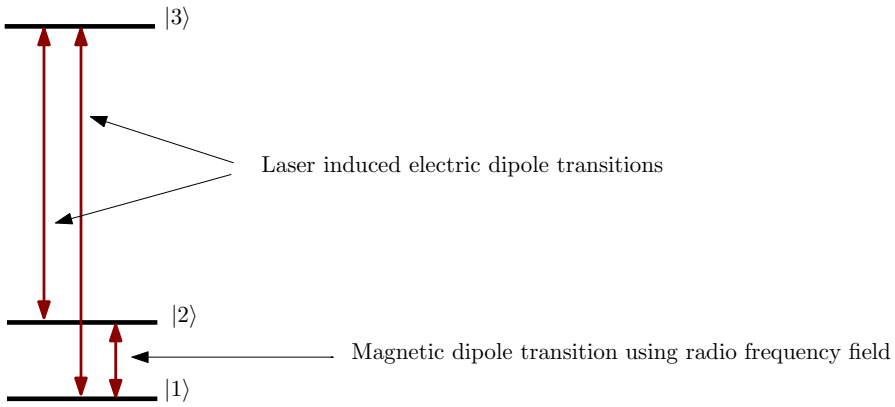

Figure 4.1: Energy level diagram of the system we are studying

Initially we will assume that the spacing between the energy levels is much larger than the line-width, i.e. an electro-magnetic field which is tuned around the frequency of the transition between level 1 and 3 will not cause excitation to the second level etc. In chapter 5 the validity of this assumption will be investigated. Furthermore, for the transitions to the upper level the electric dipole approximation is made. With these assumptions the electric dipole interaction Hamiltonian has the form:

$$V_{ED} = \begin{pmatrix} 0 & 0 & -\vec{d}_{13} \cdot \vec{E}_{13} \\ 0 & 0 & -\vec{d}_{23} \cdot \vec{E}_{23} \\ -\vec{d}^*_{13} \cdot \vec{E}_{13} & -\vec{d}^*_{23} \cdot \vec{E}_{23} & 0 \end{pmatrix}$$

where $\vec{d}_{ij}$ are elements of the dipole matrix, $\vec{d}_{ij} = -e\langle i|\vec{r}|j\rangle$ and $\vec{E}_{ij}$ are the electric fields of the lasers used to stimulate transitions between levels i and j.

$$\vec{E}_{ij}(z,t) = \vec{A}_{ij}(z,t)cos(\omega^L_{ij}t - k^L_{ij}z + \phi_{ij}(t)). \tag{4.3}$$

The laser frequency is given by $\omega^L_{ij} = \omega_{ij} + \delta_{ij}$, where the detuning δ_{ij} is assumed to be small compared to the level spacing.

The magnetic transitions are treated in an analogous manner with the magnetic dipole approximation.

$$V_{MD} = \begin{pmatrix} 0 & -\vec{\mu} \cdot \vec{B} & 0 \\ -\vec{\mu}^* \cdot \vec{B} & 0 & 0 \\ 0 & 0 & 0 \end{pmatrix}$$

$\vec{\mu}$ is the magnetic dipole moment and $\vec{B}$ is the magnetic field given by $\vec{B}(z,t) = \vec{\beta}(z,t)cos(\omega_{RF}t - k_{RF}z + \phi_{RF}(t))$

4.1.2 Rotating wave approximation

In order to allow for longer time steps in the simulations it is convenient to discard all short time fluctuations which in the long run will average to zero in the Hamiltonian.

This is called the rotating wave approximation. Consider the block of the Hamiltonian which corresponds to transitions between the lowest and the highest lying levels

$$V_{13} = -\vec{d}_{13} \cdot \vec{E}_{13}|1\rangle\langle 3| - \vec{d}^{*}_{13} \cdot \vec{E}_{13}|3\rangle\langle 1| \tag{4.4}$$

The first part of V_{13} is a lowering operator which takes state 3 to state 1 and the second part a raising operator which takes 1 to 3.

The electric field can be rewritten as (see ref. [11] for details)

$$\begin{aligned}\vec{E}_{13} =& \frac{\vec{A}_{13}(z,t)}{2}\left((e^{i(\omega^L_{13}t - k^L_{13}z)} + e^{-i(\omega^L_{13}t - k^L_{13}z)})cos(\phi(t))\right) + \\ &+ i\frac{\vec{A}_{13}(z,t)}{2}\left((e^{i(\omega^L_{13}t - k^L_{13}z)} - e^{-i(\omega^L_{13}t - k^L_{13}z)})sin(\phi(t))\right)\end{aligned} \tag{4.5}$$

From the time evolution of the basis states $\vec{d}_{13}$ will contain terms of the form $e^{i\omega_{13}t}$, $\omega_{13} = \omega_1 - \omega_3 < 0$.

The interaction will thus contain terms proportional to $e^{\pm i(\omega_{13}+\omega^L_{13})t}$ as well as $e^{\pm i(\omega_{13}-\omega^L_{13})t}$. Assuming the detuning to be small $e^{\pm i(\omega_{13}-\omega^L_{13})t}$ will be fast oscillating compared to the other terms and average to zero over longer time periods . This term can therefore be neglected. This is the so called rotating wave approximation. The same argument can be used on the complete Hamiltonian yielding the expression.

$$H = \begin{pmatrix} \hbar\omega_1 & -\frac{1}{2}(\hbar\Omega^R_{RF} + i\hbar\Omega^I_{RF})e^{i\omega_{RF}t - ik_{RF}z} & -\frac{1}{2}(\hbar\Omega^R_{13} + i\hbar\Omega^I_{13})e^{i\omega^L_{13}t - ik^L_{13}z} \\ \left(-\frac{1}{2}(\hbar\Omega^R_{RF} + i\hbar\Omega^I_{RF})e^{i\omega_{RF}t - ik_{RF}z}\right)^* & \hbar\omega_2 & -\frac{1}{2}(\hbar\Omega^R_{23} + i\hbar\Omega^I_{23})e^{i\omega^L_{23}t - ik^L_{23}z} \\ \left(-\frac{1}{2}(\hbar\Omega^R_{13} + i\hbar\Omega^I_{13})e^{i\omega^L_{13}t - ik^L_{13}z}\right)^* & \left(-\frac{1}{2}(\hbar\Omega^R_{23} + i\hbar\Omega^I_{23})e^{i\omega^L_{23}t - ik^L_{23}z}\right)^* & \hbar\omega_3 \end{pmatrix}$$

In analogy with the derivation given in ref. [11] the real and imaginary parts of Rabi frequencies have been defined in the following manner;

$$\hbar\Omega^R_{ij}(t) \equiv \vec{d}_{ij} \cdot \vec{A}_{ij} cos(\phi_{ij}(t))$$
$$\hbar\Omega^I_{ij}(t) \equiv \vec{d}_{ij} \cdot \vec{A}_{ij} sin(\phi_{ij}(t))$$

as well as

$$\hbar\Omega^R_{RF}(t) \equiv \vec{\mu} \cdot \vec{\beta} cos(\phi_{RF}(t))$$
$$\hbar\Omega^I_{RF}(t) \equiv \vec{\mu} \cdot \vec{\beta} sin(\phi_{RF}(t))$$

4.1.3 Setting up the equations

Since we will investigate ensembles of atoms the density matrix formulation of quantum mechanics will be used. The time evolution of the density matrix (ρ) is given by the Liouville equation, [14]

$$\dot{\rho} = \frac{i}{\hbar}[\rho, H] + \gamma\rho \tag{4.6}$$

Instead of defining the damping term ($\rho\gamma$) on matrix form it will be intuitively introduced by making use of the Einstein coefficients for the transitions, Γ_{ij}. The logic is as follows; the population in state 2 should increase with spontaneous decay from state 3 and decrease with spontaneous decay to state 1. This means that the damping term for ρ_{22} is given by $(\gamma\rho)_{22} = \Gamma_{23}\rho_{33} - \Gamma_{21}\rho_{22}$. The same reasoning is used for the other populations. For the coherences the damping should only depend on the corresponding transition. Thus for example $(\gamma\rho)_{23} = -\Gamma'_{23}\rho_{23}$ etc. A more rigorous motivation is given in e.g. ref. [16].

The differential equation governing the time evolution of our 3-level system is received by inserting the Hamiltonian derived in the last section in equation 4.6. It is important to note that the density matrix is Hermitian ($\rho_{21} = \rho^*_{12}$).

$$\begin{aligned}
\dot{\rho}_{11} &= \frac{i}{\hbar}(-H_{12}\rho^*_{12} + H^*_{12}\rho_{12} - H_{13}\rho^*_{13} + H^*_{13}\rho_{13}) + \Gamma_{12}\rho_{22} + \Gamma_{13}\rho_{33} \\
\dot{\rho}_{22} &= \frac{i}{\hbar}(H_{12}\rho^*_{12} - H^*_{12}\rho_{12} - H_{23}\rho^*_{23} + H^*_{23}\rho_{23}) + \Gamma_{23}\rho_{33} - \Gamma_{12}\rho_{22} \\
\dot{\rho}_{33} &= \frac{i}{\hbar}(H_{13}\rho^*_{13} - H^*_{13}\rho_{13} + H_{23}\rho^*_{23} - H^*_{23}\rho_{23}) - \Gamma_{23}\rho_{33} - \Gamma_{13}\rho_{33} \\
\dot{\rho}_{12} &= \frac{i}{\hbar}(-H_{12}(\rho_{22} - \rho_{11}) - H_{13}\rho^*_{23} + H^*_{23}\rho_{13} - (H_{11} - H_{22})\rho_{12}) - \Gamma'_{12}\rho_{12} \\
\dot{\rho}_{13} &= \frac{i}{\hbar}(-H_{13}(\rho_{33} - \rho_{11}) - H_{12}\rho_{23} + H_{23}\rho_{12} - (H_{11} - H_{33})\rho_{13}) - \Gamma'_{13}\rho_{13} \\
\dot{\rho}_{23} &= \frac{i}{\hbar}(-H_{23}(\rho_{33} - \rho_{22}) - H^*_{12}\rho_{13} + H_{13}\rho^*_{12} - (H_{22} - H_{33})\rho_{23}) - \Gamma'_{23}\rho_{23}
\end{aligned} \tag{4.7}$$

Since we're assuming the system to be closed the trace of the density matrix is conserved in the operation and thus there are only two independent diagonal elements. Defining these as

$$\begin{aligned}
n_1 &= \rho_{22} - \rho_{11} \\
n_2 &= \rho_{22} - \rho_{33}
\end{aligned} \tag{4.8}$$

the equations become:

$$\begin{aligned}
\dot{n}_1 =& \frac{2i}{\hbar}(H_{12}\rho_{12}^* - H_{12}^*\rho_{12}) - \frac{i}{\hbar}(H_{23}\rho_{23}^* - H_{23}^*\rho_{23}) + \frac{i}{\hbar}(H_{13}\rho_{13}^* - H_{13}^*\rho_{13}) \\
& - 2\Gamma_{12}\rho_{22} + \Gamma_{23}\rho_{33} - \Gamma_{13}\rho_{33} \\
\dot{n}_2 =& -\frac{2i}{\hbar}(H_{23}\rho_{23}^* - H_{23}^*\rho_{23}) + \frac{i}{\hbar}(H_{12}\rho_{12}^* - H_{12}^*\rho_{12}) - \frac{i}{\hbar}(H_{13}\rho_{13}^* - H_{13}^*\rho_{13}) \\
& 2\Gamma_{23}\rho_{33} - \Gamma_{12}\rho_{22} + \Gamma_{13}\rho_{33} \\
\dot{\rho}_{12} =& \frac{i}{\hbar}(-H_{12}n_1 - H_{13}\rho_{23}^* + H_{23}^*\rho_{13} - (H_{11} - H_{22})\rho_{12}) - \Gamma'_{12}\rho_{12} \\
\dot{\rho}_{13} =& \frac{i}{\hbar}(-H_{13}(n_1 - n_2) - H_{12}\rho_{23} + H_{23}\rho_{12} - (H_{11} - H_{33})\rho_{13}) - \Gamma'_{13}\rho_{13} \\
\dot{\rho}_{23} =& \frac{i}{\hbar}(H_{23}n_2 - H_{12}^*\rho_{13} + H_{13}\rho_{12}^* - (H_{22} - H_{33})\rho_{23}) - \Gamma'_{23}\rho_{23}
\end{aligned} \tag{4.9}$$

By finally noting that $H_{12}\rho_{12}^* - H_{12}^*\rho_{12} = 2i \cdot Im(H_{12}\rho_{12}^*)$ the diagonal elements can be further simplified yielding

$$\begin{aligned}
\dot{n}_1 =& -\frac{4}{\hbar}Im(H_{12}\rho_{12}^*) + \frac{2}{\hbar}Im(H_{23}\rho_{23}^*) - \frac{2}{\hbar}Im(H_{13}\rho_{13}^*) - 2\Gamma_{12}\rho_{22} + \Gamma_{23}\rho_{33} - \Gamma_{13}\rho_{33} \\
\dot{n}_2 =& \frac{4}{\hbar}Im(H_{23}\rho_{23}^*) - \frac{2}{\hbar}Im(H_{12}\rho_{12}^*) + \frac{2}{\hbar}Im(H_{13}\rho_{13}^*) + 2\Gamma_{23}\rho_{33} - \Gamma_{12}\rho_{22} + \Gamma_{13}\rho_{33} \\
\dot{\rho}_{12} =& \frac{i}{\hbar}(-H_{12}n_1 - H_{13}\rho_{23}^* + H_{23}^*\rho_{13} - (H_{11} - H_{22})\rho_{12}) - \Gamma'_{12}\rho_{12} \\
\dot{\rho}_{13} =& \frac{i}{\hbar}(-H_{13}(n_1 - n_2) - H_{12}\rho_{23} + H_{23}\rho_{12} - (H_{11} - H_{33})\rho_{13}) - \Gamma'_{13}\rho_{13} \\
\dot{\rho}_{23} =& \frac{i}{\hbar}(H_{23}n_2 - H_{12}^*\rho_{13} + H_{13}\rho_{12}^* - (H_{22} - H_{33})\rho_{23}) - \Gamma'_{23}\rho_{23}
\end{aligned} \tag{4.10}$$

where the diagonal elements ρ_{22} and ρ_{33} are given in terms of the new variables n_1 and n_2 as:

$$\begin{aligned}
\rho_{22} &= \frac{n_1 + n_2 + 1}{3} \\
\rho_{33} &= \frac{n_1 - 2n_2 + 1}{3}
\end{aligned} \tag{4.11}$$

4.1.4 Changing to a rotating coordinate system

The equations 4.10 are somewhat problematic when you want to solve the equations for longer time periods due to the fast oscillations of the laser. The natural time scale for atomic energies is approximately 24 as (the time-scale in atomic units) and thus the light fields will fluctuate on this time-scale. In this thesis we wish to simulate the behaviour of atomic systems on the microsecond time scale. The short-term fluctuations of the laser will thus become problematic since it requires very short time steps. This problem

can be solved by changing coordinates to a coordinate system which "rotates with the light fields".

Consider the unitary transformation given by

$$U = \begin{pmatrix} 1 & 0 & 0 \\ 0 & e^{-i(\omega_{RF}t - k_{RF}z)} & 0 \\ 0 & 0 & e^{-i(\omega_{13}^L t - k_{13}^L z)} \end{pmatrix}$$

Applying this transformation on both sides of equation 4.6 (temporary disregarding from the damping term) you get (see ref [11]).

$$\begin{aligned} U^{-1}\dot{\rho}U &= \frac{i}{\hbar}U^{-1}[\rho, H]U \\ ... &\Leftrightarrow ... \\ \dot{\tilde{\rho}} &= \frac{i}{\hbar}[\tilde{\rho}, \tilde{H} - G] \end{aligned} \tag{4.12}$$

where $G = i\hbar U^{-1}\dot{U}$ is given by

$$G = \begin{pmatrix} 0 & 0 & 0 \\ 0 & \hbar\omega_{RF} & 0 \\ 0 & 0 & \hbar\omega_{13}^L \end{pmatrix}$$

Thus if we define the effective Hamiltonian in the rotating system as $H' = \tilde{H} - G$ the time evolution of the density matrix in the rotating system is given by:

$$\begin{aligned} \dot{\tilde{n}}_1 =& -\frac{4}{\hbar}Im(H'_{12}\tilde{\rho}^*_{12}) + \frac{2}{\hbar}Im(H'_{23}\tilde{\rho}^*_{23}) - \frac{2}{\hbar}Im(H'_{13}\tilde{\rho}^*_{13}) - 2\Gamma_{12}\tilde{\rho}_{22} + \Gamma_{23}\tilde{\rho}_{33} - \Gamma_{13}\tilde{\rho}_{33} \\ \dot{\tilde{n}}_2 =& \frac{4}{\hbar}Im(H'_{23}\tilde{\rho}^*_{23}) - \frac{2}{\hbar}Im(H'_{12}\tilde{\rho}^*_{12}) + \frac{2}{\hbar}Im(H'_{13}\tilde{\rho}^*_{13}) + 2\Gamma_{23}\tilde{\rho}_{33} - \Gamma_{12}\tilde{\rho}_{22} + \Gamma_{13}\tilde{\rho}_{33} \\ \dot{\tilde{\rho}}_{12} =& \frac{i}{\hbar}(-H'_{12}\tilde{n}_1 - H'_{13}\tilde{\rho}^*_{23} + H'^*_{23}\tilde{\rho}_{13} - (H'_{11} - H'_{22})\tilde{\rho}_{12}) - \Gamma'_{12}\tilde{\rho}_{12} \\ \dot{\tilde{\rho}}_{13} =& \frac{i}{\hbar}(-H'_{13}(\tilde{n}_1 - \tilde{n}_2) - H'_{12}\tilde{\rho}_{23} + H'_{23}\tilde{\rho}_{12} - (H'_{11} - H'_{33})\tilde{\rho}_{13}) - \Gamma'_{13}\tilde{\rho}_{13} \\ \dot{\tilde{\rho}}_{23} =& \frac{i}{\hbar}(H'_{23}\tilde{n}_2 - H'^*_{12}\tilde{\rho}_{13} + H'_{13}\tilde{\rho}^*_{12} - (H'_{22} - H'_{33})\tilde{\rho}_{23}) - \Gamma'_{23}\tilde{\rho}_{23} \end{aligned} \tag{4.13}$$

The effective Hamiltonian is given explicitly as

$$H' = \begin{pmatrix} \hbar\omega_1 & -\frac{1}{2}(\hbar\Omega^R_{RF} + i\hbar\Omega^I_{RF}) & -\frac{1}{2}(\hbar\Omega^R_{13} + i\hbar\Omega^I_{13}) \\ \left(-\frac{1}{2}(\hbar\Omega^R_{RF} + i\hbar\Omega^I_{RF})\right)^* & \hbar\omega_2 - \hbar\omega_{RF} & -\frac{1}{2}(\hbar\Omega^R_{23} + i\hbar\Omega^I_{23}) \\ \left(-\frac{1}{2}(\hbar\Omega^R_{13} + i\hbar\Omega^I_{13})\right)^* & \left(-\frac{1}{2}(\hbar\Omega^R_{23} + i\hbar\Omega^I_{23})\right)^* & \hbar\omega_3 - \hbar\omega^L_{13} \end{pmatrix}$$

where, to our delight, the fast oscillating terms have vanished.

4.1.5 Analytical zero-field solution to the Bloch equations

It is instructive to look at the analytical solution to the three level Bloch equations without a field present. With no fields present the equations 4.13 simplify to

$$\begin{aligned}
\dot{\tilde{n}}_1 =& \frac{\tilde{n}_1}{3}(2\Gamma_{23} - 2\Gamma_{12} - \Gamma_{13}) + \frac{\tilde{n}_2}{3}(2\Gamma_{13} - 2\Gamma_{12} - 4\Gamma_{23}) - \frac{1}{3}(2\Gamma_{12} + 2\Gamma_{23} - \Gamma_{13}) \\
\dot{\tilde{n}}_2 =& \frac{\tilde{n}_1}{3}(2\Gamma_{23} - \Gamma_{12} + \Gamma_{13}) + \frac{\tilde{n}_2}{3}(-2\Gamma_{13} - \Gamma_{12} - 4\Gamma_{23}) - \frac{1}{3}(\Gamma_{12} + 2\Gamma_{23} + \Gamma_{13}) \\
\dot{\tilde{\rho}}_{12} =& -\frac{i}{\hbar}(H'_{11} - H'_{22})\tilde{\rho}_{12} - \Gamma'_{12}\tilde{\rho}_{12} \\
\dot{\tilde{\rho}}_{13} =& -\frac{i}{\hbar}(H'_{11} - H'_{33})\tilde{\rho}_{13} - \Gamma'_{13}\tilde{\rho}_{13} \\
\dot{\tilde{\rho}}_{23} =& -\frac{i}{\hbar}(H'_{22} - H'_{33})\tilde{\rho}_{23} - \Gamma'_{23}\tilde{\rho}_{23}
\end{aligned} \tag{4.14}$$

The last three equations are straight forward to solve but the upper two require some thinking.

By defining a vector

$$\vec{n} = \begin{pmatrix} \tilde{n}_1 \\ \tilde{n}_2 \end{pmatrix}$$

the upper two equations can be written as

$$\dot{\vec{n}} = A\vec{n} + \vec{b} \tag{4.15}$$

where A is a constant matrix given by

$$A = \frac{1}{3}\begin{pmatrix} -2\Gamma_{13} - \Gamma_{13} + \Gamma_{23} & -2\Gamma_{12} + 2\Gamma_{13} - 2\Gamma_{23} \\ -\Gamma_{12} + \Gamma_{13} + 2\Gamma_{23} & -\Gamma_{12} - 2\Gamma_{13} - 4\Gamma_{23} \end{pmatrix}$$

and $\vec{b}$ a constant vector

$$\vec{b} = \frac{1}{3}\begin{pmatrix} -2\Gamma_{12} - \Gamma_{13} + \Gamma_{23} \\ -\Gamma_{12} + \Gamma_{13} + 2\Gamma_{23} \end{pmatrix}.$$

The equation 4.15 has to be stable and converge towards $n_1 = -1$ and $n_2 = 0$ so the solution can be written as

$$\vec{n}(t) = e^{At}(\vec{n}(0) - \vec{b}^*) \tag{4.16}$$

where $\vec{b}^*$ is given by

$$\vec{b}^* = -A^{-1}\vec{b}$$

The last three equations can be integrated directly to yield

$$\begin{aligned}
\tilde{\rho}_{12}(t) &= \tilde{\rho}_{12}(0) \cdot e^{(-\frac{i}{\hbar}(H'_{11} - H'_{22}) - \Gamma'_{12})t} \\
\tilde{\rho}_{13}(t) &= \tilde{\rho}_{13}(0) \cdot e^{(-\frac{i}{\hbar}(H'_{11} - H'_{33}) - \Gamma'_{13})t} \\
\tilde{\rho}_{23}(t) &= \tilde{\rho}_{23}(0) \cdot e^{(-\frac{i}{\hbar}(H'_{22} - H'_{33}) - \Gamma'_{23})t}
\end{aligned} \tag{4.17}$$

From these equations we can see that the coherences have an oscillatory behaviour given by the level spacing as well as an exponential decay from the decoherence factors.

4.2 Two level systems and the Bloch Sphere

4.2.1 What is the meaning of the rotating coordinate system?

The rotating coordinate system greatly simplifies our calculations. However, it will also prove convenient when interpreting the result. For simplicity let us consider a two level system. A general two level system can be described by the state

$$|\Psi(t)\rangle = c_1|1\rangle e^{-i\omega_1 t} + c_2|2\rangle e^{-i\omega_2 t} \tag{4.18}$$

The transformation corresponding to U (with $z = 0$) then takes

$$|\Psi(t)\rangle \to |\Psi'(t)\rangle = c_1|1\rangle e^{-i\delta t/2} + c_2|2\rangle e^{i\delta t/2} \tag{4.19}$$

where δ is the detuning of the laser.

Using the density matrix formulation the diagonal elements are left unchanged but the coherences transforms as:

$$\begin{aligned} \rho_{12}(t) &\to \tilde{\rho}_{12}(t) = c_1 c_2^* e^{-i\delta t} \\ \rho_{21}(t) &\to \tilde{\rho}_{21}(t) = c_1^* c_2 e^{i\delta t} \end{aligned} \tag{4.20}$$

In terms of these coherences the expectation value of the dipole moment of the atom is given by [17, p. 129]

$$D(t) = d_{12}^* \tilde{\rho}_{12}(t) e^{i\omega_{12}^L t} + d_{12}\tilde{\rho}_{12}^*(t) e^{-i\omega_{12}^L t} \tag{4.21}$$

Thus the coherences in the rotating system gives the response of the atom on an applied electric field with zero detuning. Henceforth these coordinates will be used unless otherwise specified.

4.2.2 The Bloch Sphere

A very convenient representation of the evolution of a two level system is given by the so called Bloch Sphere. Defining the coordinates:

$$\begin{aligned} u &= \tilde{\rho}_{12} + \tilde{\rho}_{21} \\ v &= -i(\tilde{\rho}_{12} - \tilde{\rho}_{21}) \\ w &= \tilde{\rho}_{11} - \tilde{\rho}_{22} \end{aligned} \tag{4.22}$$

The state of a two level system can be represented as a vector

$$\vec{r} = u\vec{e}_1 + v\vec{e}_2 + w\vec{e}_3 \tag{4.23}$$

From the Bloch equations of a two level system it is straight forward to show that (see ref [17]) the Bloch vector $\vec{r}$ has the norm 1 for all pure states. Thus all pure states are situated on the surface of the so called Bloch Sphere. The more mixed the ensembles

become the more they deviate from this surface and move closer to the centre of the sphere. A completely mixed ensemble is situated in the centre of the Bloch sphere.

Assuming no de-coherence and infinite life time of the atoms the quantity $\vec{r} \cdot \vec{W}$, $\vec{W} = \Omega_{12}\vec{e}_1 + \delta\vec{e}_3$, is also preserved. Thus, if the atom is excited with radiation with constant Rabi frequency and detuning the state will precess on the Bloch sphere keeping a constant angle toward $\vec{W}$. [17, p. 131]

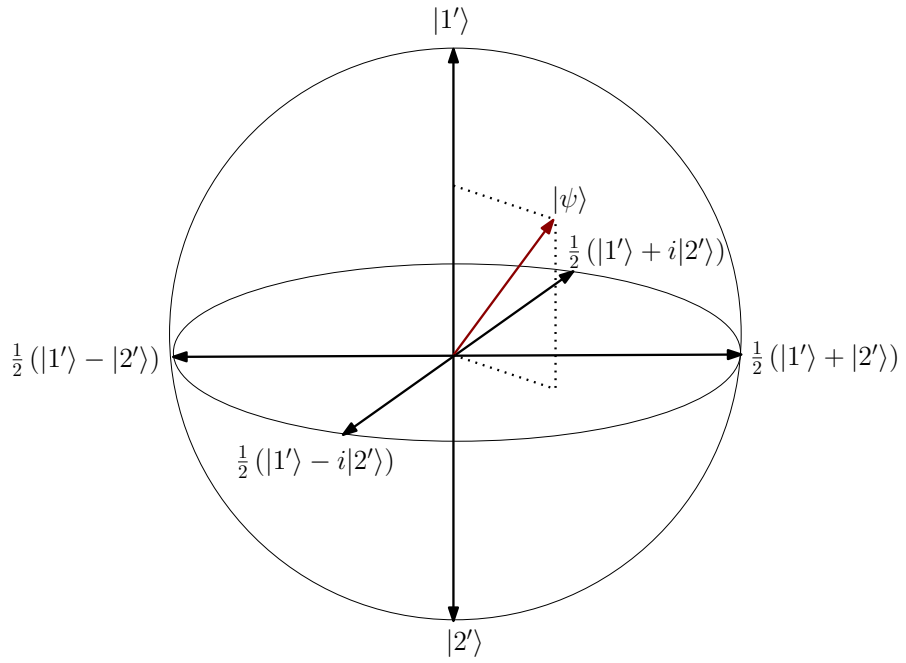

Figure 4.2: Picture of the Bloch Sphere. The prime superscript denotes that the basis states are expressed in the rotating basis.

4.2.3 Numerical simulations using the 3-level Bloch equations

The equations 4.13 are straight forward to solve numerically. In this thesis I used a fourth order Runge Kutta algorithm to solve the equations. Space was discretized in a z-mesh. Since, in the general case, both the spin and the excited states are broadened, the equations were solved for all detunings of the spin and excited states. Thus four nested loops are required, one going over z, one over the detunings of the excited state, one over the detunings of the spin state and the innermost over time.

The Bloch equations are convenient to use in order to investigate population transfer for given input pulses. That is, if you start with a given state of the system represented by a given density matrix, you let the system interact with electric fields of specified frequencies, amplitudes and phase, the Bloch equations will give you the density matrix of the system after the interaction.

However, the main goal of this project was to investigate the efficiency of different quantum memory schemes. The efficiency is defined as the ratio between the energy of the outgoing echo pulse and the energy of the incoming data pulse. For this purpose the Bloch equations alone are useless since they only describe how the material reacts on the applied fields. The echo pulse is a result of the opposite interaction, how the polarization of the material affects the electric field. Since we use a semi-classical model where the electric field is treated as a classical field the equations governing the time evolution of the fields are the Maxwell equations.

4.3 Including spatial dependence of the electric fields; Solving the Maxwell wave equations

The derivation in this section is a generalization of the derivation for a two-level system given in ref. [11].

4.3.1 Initial definitions

There are two different types of fields which we use. Laser fields, approximated as electric dipole fields, that are used to excite the atoms to the optical level $|3\rangle$, and a radio frequency field, approximated as a magnetic dipole field which is used to stimulate transitions between the two ground state hyperfine levels. However, since the wavelengths of the RF-pulses are long compared to the size of the crystal, propagation effects for these fields do not need to be taken into account. In the derivations below we thus only care about the electric fields corresponding to the $|1\rangle \leftrightarrow |3\rangle$ and $|2\rangle \leftrightarrow |3\rangle$ transitions.

4.3.2 Setting up the Maxwell equations

Our system is given by rare earth ions doped into an inorganic crystal. This is a non-magnetic and to a good approximation homogeneous medium and thus the magnetization $\vec{M} = 0$ and $\vec{\nabla} \cdot \vec{E} = 0$. Moreover the ohmic loss will be assumed to be zero in the material which is equivalent to the assumption that the material is non-conducting. Since the host materials we are investigating are very insulating this is a good approximation.

The Maxwell equations for such a system is given by ([18, p. 237]):

$$\vec{\nabla} \times \vec{H} = \frac{dD}{dt} \tag{4.24}$$

$$\vec{\nabla} \times \vec{E} = -\frac{dB}{dt} \tag{4.25}$$

$$\vec{\nabla} \cdot \vec{D} = 0 \tag{4.26}$$

$$\vec{\nabla} \cdot \vec{B} = 0 \tag{4.27}$$

The dielectric flux $\vec{D}$ is given by

$$\vec{D} = \epsilon \vec{E} + \vec{P}_{total} \tag{4.28}$$

where ϵ is the dielectric permeability of the material and $\vec{P}_{total}$ the total polarization,

$$\vec{P}_{total} = \vec{P}_{host} + \vec{P}. \tag{4.29}$$

The polarization of the host material will, since it's optically transparent and insulating, be linear

$$\vec{P}_{host} = \epsilon\chi\vec{E} \tag{4.30}$$

For the same reason the magnetization will be zero which gives the following relation between the magnetic field H and the magnetic flux B;

$$B = \mu H \tag{4.31}$$

where μ is the magnetic permeability of the host material.

It is straight forward to show (see eg. [11], [19, p 814]) that for these assumptions the Maxwell equations combine to give the following wave equation for the electric field.

$$\Delta\vec{E} - \frac{n^2}{c^2}\frac{d^2\vec{E}}{dt^2} = \mu\frac{d^2\vec{P}}{dt^2}. \tag{4.32}$$

Here, $\vec{P}$ is the non-linear part of the polarization of the material and the refractive index n is defined as $n^2 = (1+\chi)$.

Thus, the effect of the ions on the electric field is contained in the polarization of the ions.

4.3.3 Calculating the total Polarization of the ions

In equation 4.21 the dipole moment for a transition in a single ion is given. The Polarization is the dipole moment per unit volume. The macroscopic dipole moment is given by the sum of the microscopic dipole moments, and thus for two level atoms, the total polarization is given by [18, p. 152], [19, p. 815], [20, p. 36]

$$\vec{P}_{i3}(z,t) = \frac{\mathcal{N}}{2\pi}\int_{-\infty}^{\infty} g(\delta)D_{i3}(\delta,z,t)d\delta. \tag{4.33}$$

Here i takes the values 1,2 and $g(\delta)$ is the inhomogeneous spectral profile as a function of the detuning from the free ion energy level and $\mathcal{N}$ the density of atomic dipoles. D_x is given by the same expression as before, only that here also the spatial dependence is included.

$$\begin{aligned} D_{i3}(\delta,z,t) =& d^*_{i3}\tilde{\rho}_{i3}(\delta,t)e^{i(\omega^L_{i3}t-k^L_{i3}z)} + d_{i3}\tilde{\rho}^*_{i3}(\delta,t)e^{-i(\omega^L_{i3}t-k^L_{i3}z)} \\ =& d^*_{i3}(u_{i3}(\delta,t) + iv_{i3}(\delta,t))e^{i(\omega^L_{i3}t-k^L_{i3}z)} + cc \end{aligned} \tag{4.34}$$

where u , v are the Bloch vectors for the two level system as defined in equation 4.22.

The inhomogeneous spectral profile is normalized as [19, 11]

$$\int_{-\infty}^{\infty} g(\delta)d\delta = 2\pi. \tag{4.35}$$

For 3-level atoms the detunings of both state 2 (the spin state) and state 3 (the optical state) has to be taken into consideration since the state of the atom will be a function of both these parameters. Equation 4.33 then generalizes to

$$\vec{P}_{i3}(z,t) = \frac{\mathcal{N}}{2\pi}\int_{-\infty}^{\infty}\int_{-\infty}^{\infty} g(\delta)g_s(\Delta)D_{i3}(\delta,\Delta,z,t)d\delta d\Delta \tag{4.36}$$

with the normalization

$$\int_{-\infty}^{\infty}\int_{-\infty}^{\infty} g(\delta)g_s(\Delta)d\delta d\Delta = 2\pi. \tag{4.37}$$

4.3.4 Rewriting the equations in terms of the Rabi frequencies

The electric field is given in terms of the Rabi frequencies as

$$E_{i3}(z,t) = \frac{\hbar}{2d_{i3}}(e^{i(\omega_{i3}^L t - z_{i3}^L)}(\Omega_{i3}^R + i\Omega_{i3}^I) + cc) \tag{4.38}$$

Inserting this equation in equation 4.32 the following equation for the Rabi frequencies is received;

$$\frac{\hbar}{2d_{i3}}(\Delta - \frac{n^2}{c^2}\frac{d^2}{dt^2})(e^{i(\omega_{i3}^L t - z_{i3}^L)}(\Omega_{i3}^R + i\Omega_{i3}^I) + e^{-i(\omega_{i3}^L t - z_{i3}^L)}(\Omega_{i3}^R - i\Omega_{i3}^I)) = \mu\frac{d^2\vec{P}}{dt^2}. \tag{4.39}$$

Assuming the Rabi frequency to be slowly varying compared to the laser frequency the terms containing $\frac{d^2\Omega}{dt^2}$ will be much smaller than the other terms and can thus be neglected. This is called the slowly varying envelope approximation. Using the fact that $k^L = \omega^L n/c$ the same reasoning can be used for the spatial derivatives. With this approximation the left hand side of equation 4.39 can be simplified to [11]

$$LHS \approx \frac{-i\omega_{i3}^L\hbar}{d_{i3}}e^{i(\omega_{i3}^L - z_{i3}^L n/c)}\left(\frac{n_z}{c}\frac{d}{dz}(\Omega_{i3}^R + i\Omega_{i3}^I) + \frac{n_z^2}{c^2}\frac{d}{dt}(\Omega_{i3}^R + i\Omega_{i3}^I)\right) + cc. \tag{4.40}$$

In the equation above it has been assumed that the axes have been chosen so that n is diagonal. n_z is then the component of n corresponding to the z-direction.

The right hand side of the equation can also be further simplified by making use of the slowly varying envelope approximation [11].

$$RHS \approx -\frac{(\omega_{i3}^L)^2}{4}\pi\mu\mathcal{N}e^{i(\omega_{i3}^L - z_{i3}^L n/c)}\int_{-\infty}^{\infty}\int_{-\infty}^{\infty} g(\delta)g_s(\Delta)(u_{i3}(\delta,\Delta,t)+iv_{i3}(\delta,\Delta,t))d_{i3}^* d\delta d\Delta + cc \tag{4.41}$$

Setting the RHS equal to the LHS and matching the real and imaginary parts the following equations for the Rabi frequencies are obtained;

$$\begin{aligned}\frac{d\Omega_{i3}^R}{dz} + \frac{n}{c}\frac{d\Omega_{i3}^R}{dt} &= \frac{\alpha}{2\pi}\int_{-\infty}^{\infty}\int_{-\infty}^{\infty} g(\delta)g_s(\Delta)v_{i3}d\delta d\Delta \\ \frac{d\Omega_{i3}^I}{dz} + \frac{n}{c}\frac{d\Omega_{i3}^I}{dt} &= -\frac{\alpha}{2\pi}\int_{-\infty}^{\infty}\int_{-\infty}^{\infty} g(\delta)g_s(\Delta)u_{i3}d\delta d\Delta.\end{aligned}$$

α is the absorption coefficient and is given by $\alpha = \frac{|d_{i3}|^2 \omega_{i3}^L \mathcal{N}}{2c\hbar n\epsilon}$.

However, since we are studying a three level system the Bloch vector representation is not that useful. The equations above can therefore be re-expressed in the coherences.

$$\frac{d\Omega_{i3}^R}{dz} + \frac{n}{c}\frac{d\Omega_{i3}^R}{dt} = \frac{\alpha}{\pi}\int_{-\infty}^{\infty}\int_{-\infty}^{\infty} g(\delta)g_s(\Delta)Im(\tilde{\rho}_{i3})d\delta d\Delta \tag{4.42}$$

$$\frac{d\Omega_{i3}^I}{dz} + \frac{n}{c}\frac{d\Omega_{i3}^I}{dt} = -\frac{\alpha}{\pi}\int_{-\infty}^{\infty}\int_{-\infty}^{\infty} g(\delta)g_s(\Delta)Re(\tilde{\rho}_{i3})d\delta d\Delta \tag{4.43}$$

4.3.5 Retarded time

As usual in electromagnetism a transformation to so called retarded time coordinates will prove convenient. This corresponds to the transformation $t \to \tau = t - \frac{zn}{c}$, $z \to z'$. The derivatives transform as

$$\frac{d}{dt} \to \frac{d}{d\tau} \tag{4.44}$$

$$\frac{d}{dz} \to -\frac{n}{c}\frac{d}{d\tau} + \frac{d}{dz'} \tag{4.45}$$

Since the time derivative is left unchanged in the transformation the Bloch equations have the same form in the retarded coordinates. The Maxwell equations, however, are greatly simplified.

$$\frac{d\Omega_{i3}^R}{dz'} = \frac{\alpha}{\pi}\int_{-\infty}^{\infty}\int_{-\infty}^{\infty} g(\delta)g_s(\Delta)Im(\tilde{\rho}_{i3})d\delta d\Delta \tag{4.46}$$

$$\frac{d\Omega_{i3}^I}{dz'} = -\frac{\alpha}{\pi}\int_{-\infty}^{\infty}\int_{-\infty}^{\infty} g(\delta)g_s(\Delta)Re(\tilde{\rho}_{i3})d\delta d\Delta \tag{4.47}$$

4.3.6 Choosing a different normalization of the inhomogeneous spectral profile

From equations 4.47 one can see that α and $g(\omega)g_s(\omega)$ will always appear as a product in the equations. We are therefore free to choose the normalization in order to minimize numerical errors. For this reason the following normalization will be used

$$\alpha g(\omega_0) = \alpha^p(\omega_0) \tag{4.48}$$

$$\int_{-\infty}^{\infty} g_s(\Delta)d\Delta = 1 \tag{4.49}$$

Here $\alpha^p(\omega_0)$ is the absorption at the specific frequency ω_0. If the normalization in equation 4.35 is kept α will be the frequency integrated absorption coefficient (see e.g. [20, p. 37]). However, for numerical reasons it will prove convenient to instead define $\max(g)$=1 and thus let $\alpha = \alpha^p(\omega_0)$ where it is understood that the maximum value of g occurs at the frequency ω_0.

The reason for this particular choice is that it avoids division followed by multiplication of a big number which introduces large numerical errors, as well as it makes the model behave correctly in the limit $g_s(\Delta) \to \delta(0)$.

4.3.7 Final equations in a rotating retarded coordinate system

Below the final Maxwell Bloch equations in a rotating retarded coordinate system are given.

$$
\begin{aligned}
\dot{\tilde{n}}_1 =& -\frac{4}{\hbar} Im(H'_{12}\tilde{\rho}^*_{12}) + \frac{2}{\hbar} Im(H'_{23}\tilde{\rho}^*_{23}) - \frac{2}{\hbar} Im(H'_{13}\tilde{\rho}^*_{13}) - 2\Gamma_{12}\tilde{\rho}_{22} + \Gamma_{23}\tilde{\rho}_{33} - \Gamma_{13}\tilde{\rho}_{33} \\
\dot{\tilde{n}}_2 =& \frac{4}{\hbar} Im(H'_{23}\tilde{\rho}^*_{23}) - \frac{2}{\hbar} Im(H'_{12}\tilde{\rho}^*_{12}) + \frac{2}{\hbar} Im(H'_{13}\tilde{\rho}^*_{13}) + 2\Gamma_{23}\tilde{\rho}_{33} - \Gamma_{12}\tilde{\rho}_{22} + \Gamma_{13}\tilde{\rho}_{33} \\
\dot{\tilde{\rho}}_{12} =& \frac{i}{\hbar}(-H'_{12}\tilde{n}_1 - H'_{13}\tilde{\rho}^*_{23} + H'^*_{23}\tilde{\rho}_{13} - (H'_{11} - H'_{22})\tilde{\rho}_{12}) - \Gamma'_{12}\tilde{\rho}_{12} \\
\dot{\tilde{\rho}}_{13} =& \frac{i}{\hbar}(-H'_{13}(\tilde{n}_1 - \tilde{n}_2) - H'_{12}\tilde{\rho}_{23} + H'_{23}\tilde{\rho}_{12} - (H'_{11} - H'_{33})\tilde{\rho}_{13}) - \Gamma'_{13}\tilde{\rho}_{13} \\
\dot{\tilde{\rho}}_{23} =& \frac{i}{\hbar}(H'_{23}\tilde{n}_2 - H'^*_{12}\tilde{\rho}_{13} + H'_{13}\tilde{\rho}^*_{12} - (H'_{22} - H'_{33})\tilde{\rho}_{23}) - \Gamma'_{23}\tilde{\rho}_{23} \\
\frac{d\Omega^R_{i3}}{dz'} =& \frac{\alpha}{\pi}\int_{-\infty}^{\infty}\int_{-\infty}^{\infty} g(\delta)g_s(\Delta)Im(\tilde{\rho}_{i3})d\delta d\Delta \\
\frac{d\Omega^I_{i3}}{dz'} =& -\frac{\alpha}{\pi}\int_{-\infty}^{\infty} g(\delta)g_s(\Delta)Re(\tilde{\rho}_{i3})d\delta d\Delta
\end{aligned}
\tag{4.50}
$$

Chapter 5

The Atomic Frequency Comb Quantum Memory

In this work I use the equations derived in last section to investigate rare-earth-ion-doped-crystal-based AFC quantum memory protocols. The efficiency of a quantum memory can be defined as the ratio between the integrated intensity of the echo pulse and the incoming pulse.

$$\eta \equiv \frac{\int |E_{echo}|^2 dt}{\int |E_{inc}|^2 dt} \tag{5.1}$$

5.1 Atomic frequency comb (AFC) - memories

AFC memories makes use of a homogeneously broadened ensemble of ions with a narrow homogeneous line width, typically rare earth ions doped into inorganic crystals. The ions are assumed to have four energy levels relevant for describing the storage process, $|aux\rangle$, $|g\rangle$, $|e\rangle$ and $|s\rangle$. $|aux\rangle$ is used as an off-level. $|g\rangle$ and $|s\rangle$ are typically different ground-state hyperfine-levels ($|1\rangle$ and $|2\rangle$ in the previous section).

The broadened ensemble is shaped into a frequency comb of equally spaced, narrow peaks in the absorption profile by optically pumping ions with certain specific level spacings to the aux-level. The FWHM of the peaks is small compared to the distance between the peaks. It can then be shown that an incoming light pulse with spectral bandwidth larger than the periodicity of the comb but smaller than the total broadening of the ensemble will interact with the comb structure to produce an echo-pulse $2\pi/\Delta$ s. later, where Δ is the spacing between the peaks. [8]

That one can reach complete absorption even though the absorption profile has a comb-like structure can be understood from the Heisenberg uncertainty principle. For short light pulse durations the absorption profile will appear smeared and complete absorption is possible.

The echo pulse is best understood in terms of the re-phasing of the ions. Since the energy levels are different for the different ions the time evolution of the system will cause a re-phasing. i.e different ions will evolve with different phases due to the

difference in energy between the excited levels. When the photon is absorbed it will be stored collectively by all ions. The state of the system is then given by so called Dicke state [21] (Assuming the pulse comes in at $t = 0$.)

$$|\Psi\rangle = \sum_j c_j e^{i\delta_j t} e^{-ikz_j} |g_1 ... e_j ... g_N\rangle \tag{5.2}$$

δ is the detuning of the atomic levels relative the central frequency, z_j the spatial position of atom j, k the wave number of the incoming radiation and c_j the amplitude for that specific mode.

Since the ions have different detunings the state will quickly de-phase after absorption. This will cause the ions to have a very low probability to decay. Assuming narrow peaks the ions will be in phase again and the original state restored at time $t = n \cdot 2\pi/\Delta$, where n is an integer, which with a certain probability will cause the echo-pulse to be emitted in the forward direction.

One quantity which will be frequently referred to is the finesse of the AFC structure. The finesse is defined as the ratio between the peak separation and the FWHM of the absorption peaks, $F = \Delta/\gamma$.

5.1.1 Why is the pulse emitted in the forward direction?

When an ion is de-excited spontaneously a photon can be emitted in an arbitrary direction. Why then is the echo pulse always emitted in the forward direction?

From a macroscopic perspective the forward propagating echo can be understood from the coupling between the forward propagating electric field to the forward propagating atomic polarization and vice versa.

However, a more intuitive explanation is given by phase matching arguments. Since we have emission from many atoms distributed in space the emission will only add constructively in certain directions, due to a phase matching process. For a large number of atoms the diffraction angle is given by $sin(\theta) \approx \lambda/d$, where d is the size of the volume.[20, p. 37] Thus, for large volumes compared to the wavelength the diffraction angle will be small and the light will be emitted coherently in the forward direction.

5.1.2 Controlling the time of the echo by making use of control pulses

In order to allow for on-demand read out, which is necessary in quantum repeaters, one can transfer the excited state $|e\rangle$ to a ground state spin level, $|s\rangle$, using a pi-pulse. The spin states do not to have a comb structure since, for the rare-earth-doped-ions considered, the spin and the optical inhomogeneous broadenings are uncorrelated. That is, the comb structure is transition specific since the inhomogeneities in the crystal affect hyperfine levels and electronically excited levels differently.

The spin state is also assumed to lie close in energy to $|g\rangle$. If this is the case the inhomogeneous broadening of the spin-state will be small compared to the AFC peak

spacing. Thus, for short term storage, the relative phase shift acquired during the spin-state storage is small.

When one wants to release the echo, the state is re-transferred to $|e\rangle$ using an other pi-pulse. The echo is then released at time $T_s + 2\pi/\Delta$, where T_s is the time difference between first and the second pi-pulse. The procedure is shown in figure 5.1.

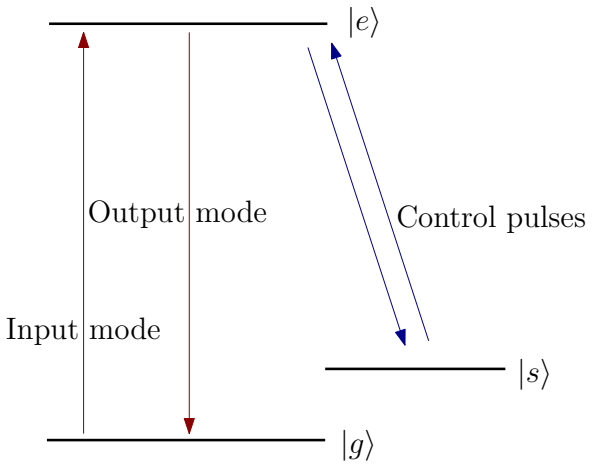

Figure 5.1: Schematic figure of the AFC process with spin-state storage.

5.1.3 Is a semi-classical treatment valid?

From discussion in the last section it is not obvious that the semi-classical model used in this work is applicable to the AFC memory scheme. In a collective Dicke state a single photon is stored in a multiple number of atoms which could indicate strong coupling between the oscillation modes of the atoms. For strong coupling the linearised MB equations derived in last section are no longer applicable. However, for the pulses we consider in this work the total population in the exited state will be negligible (probability to measure an electron in state $|e\rangle$ is small), and thus the coupling between the oscillator modes will be weak which implies that the linearised Maxwell Bloch model can be used. In a linearised MB model one basically treats the atoms as uncoupled classical oscillators whose dipole moment is given by a quantum mechanical treatment using the Bloch equations.

The linearity of the model also implies the equivalence between single photon dynamics and classical dynamics [8]. In other words the particle nature of the electric field is negligible and for large ensembles the probability distribution received from a single photon treatment is equivalent to the intensity received from a classical field point of view.

5.1.4 Forward and backward propagating echo, Analytical calculations

Afzelius et. al. [8] have investigated the AFC memory analytically by solving the linearised Maxwell Bloch equations from the last chapter for a 2-level system under the following assumptions:

- Neglect population relaxation and de-coherence for the optical transition. This is a reasonable assumption as long as the inhomogeneous broadening of the AFC peaks is larger than the homogeneous broadening.
- The efficiency of the control pulses is unity and off-resonant excitation effects are negligible.
- The hyperfine transition is de-coherence free. Also the population relaxation for the hyperfine levels are neglected.
- The hyperfine levels have no inhomogeneous broadening.
- The bandwidth of the incoming photon is smaller than the width of the spectral pit but much larger than the width of the AFC peaks. This assumption is equivalent to the motivation of the photon smearing due to Heisenberg uncertainty relation made in the last section.

For the above assumptions the linearised Maxwell-Bloch equations for a two level atom are, within the rotating wave approximation, given by [8, 22]

$$\frac{\partial}{\partial t}\sigma_f(z,t;\delta) = -i\delta\sigma_f(z,t;\delta) + id_{ge}E_f(z,t) \tag{5.3}$$

$$\frac{\partial}{\partial t}\sigma_b(z,t;\delta) = -i\delta\sigma_b(z,t;\delta) + id_{ge}E_f(z,t) \tag{5.4}$$

$$\left(\frac{\partial}{\partial t} + c\frac{\partial}{\partial z}\right)E_f(z,t) = id_{ge}\int_{-\infty}^{\infty} d\delta n(\delta)\sigma_f(z,t;\delta) \tag{5.5}$$

$$\left(\frac{\partial}{\partial t} + c\frac{\partial}{\partial z}\right)E_b(z,t) = id_{ge}\int_{-\infty}^{\infty} d\delta n(\delta)\sigma_b(z,t;\delta). \tag{5.6}$$

Here both the electric field and the atomic polarization is divided into forward and backward propagating parts (E_f , σ_f and E_b , σ_b respectively). d_{ge} is the dipole moment for the transition, δ the detuning and $n(\delta)$ the spectral distribution normalized as $\int_{-\infty}^{\infty} d\delta n(\delta) = N$, where N is the number of atoms.

The analytical calculation in ref. [8] then shows that the amplitude of the forward propagating mode after a crystal of length L is given by

$$E_f(L,t) = E_f(0,t)e^{-\tilde{\alpha}L/2} \tag{5.7}$$

where the effective absorption coefficient is defined as $\tilde{\alpha} = \frac{\alpha}{F}\sqrt{\frac{\pi}{4ln(2)}} \approx \frac{\alpha}{F}$.

If the control pulses are co-propagating the atomic polarization will be coupled to the forward propagating field mode and the photon echo will be emitted in the forward direction. Then the amplitude of the echo will be limited by absorption and the maximum efficiency is limited to 54%. If one instead would use counter propagating control fields the coupling of the atomic polarization would switch to the backward propagating mode [8, 23]. Although there will be absorption also for the backward propagating echo this effect will be overridden by the constructive interference between all possible paths of the photon in the material (i.e. all possible turning points of the photon which is summed over in the integral in the expression below) allowing for efficiencies up to unity.

$$E_{out} = -E_{in}e^{-\tilde{\gamma}^2(2\pi/\Delta)^2/2}\int_0^L dz'\tilde{\alpha}e^{-\tilde{\alpha}z'/2}e^{-\tilde{\alpha}z'/2} = -E_{in}e^{-\gamma^2(2\pi/\Delta)^2/2}(1-e^{-\tilde{\alpha}L}) \quad (5.8)$$

where $\tilde{\gamma}$ is the individual peak width which is related to the FWHM peak width as $\gamma = \sqrt{8ln(2)}\tilde{\gamma}$ For a forward propagating echo the corresponding integral would look like

$$\int_0^L dz'\tilde{\alpha}e^{-\tilde{\alpha}z'/2}e^{-\tilde{\alpha}(L-z)'/2} = \tilde{\alpha}Le^{-\tilde{\alpha}L/2} \quad (5.9)$$

Thus, for a forward propagating echo there is no such interference effect and the absorption limits the efficiency. The maximum intensity of the echo in the forward direction is received at the effective absorption depth $\tilde{d} = \tilde{\alpha} \cdot L = 2$. [8, 22]

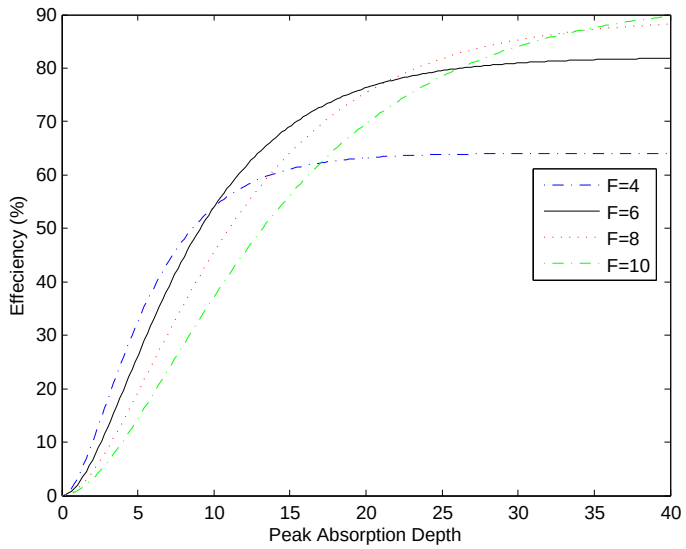

Figure 5.2: Efficiency as a function of peak absorption depth (αL) for AFC structures of different finesse, from equation 5.8.

5.2 Including spin decoherence and broadening of spin level

In order to account for decoherence and inhomogeneous broadening of the spin transition additional loss factors need to be introduced. In the equations above the loss factor is given by $e^{-\gamma^2(2\pi/\Delta)^2/2}$. This can be made arbitrary small as the finesse increases. The inhomogeneous broadening of the spin level should introduce further decoherence in the same way as above. In the derivations preceding equation 5.8 Afzelius et. al. [8] showed that the decay of the echo is given by the Fourier transform of the absorption peaks. Analogously, the decay of the echo due to the inhomogeneous broadening of the spin state should be given by the Fourier transform of the broadening. For the rare earth ion doped crystal considered in this work the broadening is Gaussian with an approximate FWHM of 26kHz,

$$n(\delta) \propto e^{-\delta^2/(2c^2)} \tag{5.10}$$

where $c = 26000 \cdot / \left(2\sqrt{2ln(2)}\right)$Hz.

Taking the Fourier transform of the broadening we see that the decay is given by

$$\eta(t) \propto e^{-2c^2\pi^2t^2} \approx e^{-2\cdot(FWHM/4.7)^2\pi^2t^2} \tag{5.11}$$

5.2.1 Compensating for the spin decoherence using RF-pulses

For the AFC memory that makes use of two control pulses it was assumed that the relative phase shift acquired when the state is stored in an inhomogenously broadened hyperfine level was negligible. However, for long time storage this is not true. In order to compensate for this phase shift it is possible to use radio-frequency-pulses (RF-pulses) to invert the population in the spin and the ground state twice. In this way the state will only change by a total phase during the spin storage and thus the time evolution of the state will be unchanged once a second control pulse re-transfers the population to the excited state. The storage time is with this scheme mainly limited by the coherence time of the hyperfine levels, which for Pr doped Y_2SiO_5 is approximately 500μs for the considered doping concentrations. This can however be extended to the order of tens or hundreds of ms by making use of the so called ZEFOZ technique.

5.2.2 ZEFOZ

As mentioned above one of the limiting parameters of the spin-wave storage quantum memory is the coherence time of the hyperfine level. The main mechanism that reduces the coherence time is magnetic interaction with the surrounding Yttrium ions. Fluctuations in this field, either due to spin-flips or due to spin exchange among the Yttrium ions reduce the coherence time of the hyperfine Pr levels drastically. The idea with the ZEFOZ technique is then to apply an external magnetic field so that the first order derivative of the Zeeman splitting becomes zero. In this way the effect of small fluctuations of the magnetic field is minimized. Using this technique the coherence time of the hyperfine levels was extended to first 82 ms and later 860 ms. [24, 25, 26]

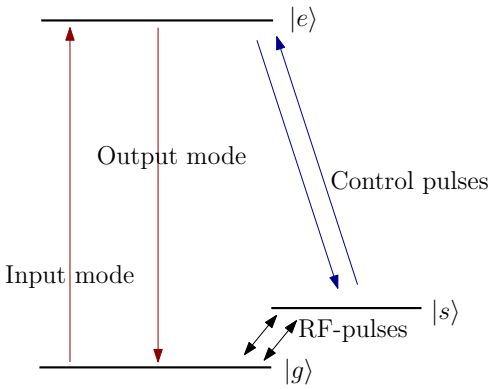

Figure 5.3: Schematic figure of the AFC process with control and RF-pulses.

5.2.3 Multi-mode capacity

One of the main advantages with the AFC memory, compared with other similar memory schemes is that it has excellent multi-mode capacity that is independent of the absorption depth of the material used. The number of possible modes in an AFC memory is proportional to the number of AFC-peaks [8], thus adding more AFC peaks allows you to store more modes. High multi-mode capacity is essential in order to achieve good quantum repeaters and thus the AFC memory is a good candidate for these applications.[8]

5.2.4 Cavity based AFC

By also making use of a cavity Afzelius et. al. [27, 28] suggested a scheme which could give efficiencies close to 1 by achieving full absorption through impedance matching. I will not, however, go through this scheme in detail. In ref. [11] numerical simulations of this scheme showed that efficiencies of 90% could be reached under perfect circumstances with a 2-level AFC-protocol of finesse 10.

The scheme was recently realized experimentally by the quantum information group at Lund university reaching efficiencies around 20%. However, it should be possible to increase the experimental efficiency quite drastically [29].

5.3 Transfer pulse types

In this work I mainly use two types of transfer pulses, Sechyp and Sechscan pulses. The advantages with these pulses is that they give good inversions for broad ensembles.

5.3.1 Square pulses

From the two level Bloch equations with infinite life and coherence times one can derive the probability of being in the upper state as [17, p. 128]

$$|c|^2 = \frac{\Omega^2}{\Omega^2 + \delta^2} sin^2 \left(\frac{\sqrt{\Omega^2 + \delta^2} t}{2} \right), \tag{5.12}$$

where δ is the detuning of the applied constant, monochromatic electric field. Thus, a pulse with a pulse area of $\Omega t = \pi$ and zero detuning will give complete transfer to the upper level. This is a so called pi-pulse. However with increasing detuning the transfer efficiency will decrease and oscillate like a sinc-function. Thus, for broadened ensembles simple square pulses will not give optimum transfer efficiency.

5.3.2 Complex Hyperbolic Secant pulses (Sechyp pulses)

A pulse better suited for broadened ensembles is the so called Sechyp-pulse. This is a complex hyperbolic secant pulse whose Rabi-frequency is given by

$$\Omega(t) = \Omega_0 \left[sech(\beta(t - t_0)) \right]^{1+i\mu}. \tag{5.13}$$

The parameter β is related to the duration and μ to the frequency chirp of the pulse which is centred at time t_0. The reason that this pulse gives a more effecient transfer than the simple square pulse is that it scans over a certain frequency width given by $\mu\beta/\pi$. The intensity FWHM of the pulse is given by $\frac{1.76}{\beta}$ and the amplitude FWHM by $\frac{2.6}{\beta}$. These pulses give good transfer rates as long as $\mu > 2$ and $\beta\mu \leq \Omega_0$. [20, p. 47],[30, p. 30-31],[31] The frequency and amplitude dependence of the sechyp pulse can be seen in figure 5.4.

5.3.3 Sechscan pulses

As can be seen in figure 5.4 the frequency dependence of the sechyp pulse is linear around t_0. It thus seems reasonable that the frequency sweep of the sechyp pulse can be extended by increasing the linear sweep around t_0. This is exactly what is done in the so called sechscan pulse. By keeping the maximum Rabi-frequency constant and extending the linear sweep around t_0 a sechscan pulse can be used to invert broader ensembles than the regular sechyp pulse (see figures 6.6-6.7).

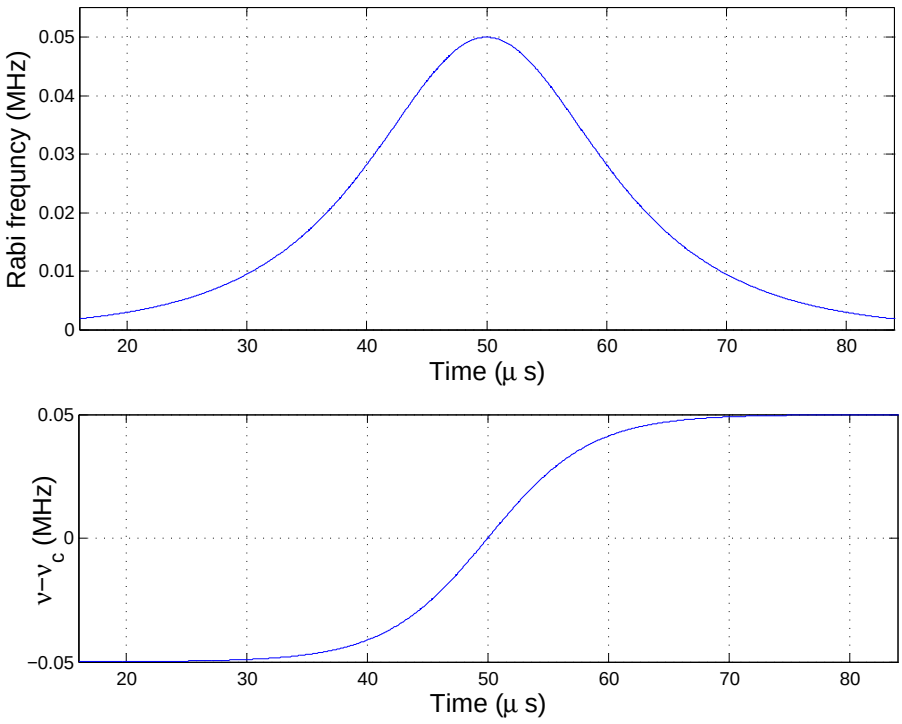

Figure 5.4: Amplitude (top) and frequency (bottom) dependence of a sechyp pulse tried for the RF transfer.

Chapter 6

Analytical Estimations and Numerical simulations

6.1 Method and Resolution Parameters

6.1.1 AFC-peak type

The calculations and measurements made in ref. [32] imply that square shaped AFC peaks gives the highest efficiency memories. This can be understood intuitively by noting that a square shaped comb maximizes the efficient absorption for a given finesse. In the lab, however, square shaped combs are hard to achieve and therefore the calculations in this section will be made with Gaussian and Super Gaussian combs of order 10. A super Gaussian function of order n is given by $A \cdot exp(-x^{2n}/(2c^{2n}))$, where A is the amplitude and c is related to the FWHM as FWHM $= 2\sqrt{2ln(2)}c$.

6.1.2 Numerical method

In order to solve the Maxwell-Bloch equations derived in previous sections four nested loops were required. The innermost loop runs over retarded time, τ, and here the Bloch equations are solved using a fourth order Runge-Kutta algorithm. The two middle loops goes over the detunings of the spin and optical state, respectively. For the optical state an AFC absorption profile was used and the spin state was assumed to have a gaussian inhomogenous broadening with a FWHM of 26 kHz. The outermost loop goes over the spatial position, z, and here the Maxwell equations were solved using a two step Adams Bashfourth method (see e.g [33, p. 190]).

6.1.3 Off resonant excitation effects

In the initial programs all off-resonant excitation effects were neglected. In this section I show that off resonant excitations due to the control pulses can effect the result and therefore should be investigated.

Off resonant excitations for the control pulses

The frequency width of a sechup pulse sweep is given by $\nu_{width} = \frac{\beta\mu}{\pi}$. To avoid resonant transitions to the wrong level for Pr doped crystals it is thus sufficient that the control pulses satisfy

$$\beta\mu < (10.2 \cdot 10^6 + \Delta\nu_{spin}) \cdot \pi, \tag{6.1}$$

where $\Delta\nu_{spin}$ is the inhomogeneous broadening of the spin state.

However, the transition between the ground state and the excited state can still be driven off-resonantly by the control pulses. The control pulses have a maximum Rabi frequency of approximately 2 MHz.

From equation 5.12 one can see that the maximum effect of off resonant excitation is then given by

$$|1\rangle \rightarrow c_1|g\rangle + \frac{\Omega}{\sqrt{\Omega^2 + \delta^2}}|3\rangle \approx 0.98|g\rangle + 0.20|e\rangle e^{i\delta'}$$

However, if smooth sechyp pulses are used the off resonant population will be driven up to the excited state and then back down again. This reduces the effect of off resonant transitions but it could still introduce a phase shift. The size of the phase shift can be investigated using simple Maxwell-Bloch 2-level simulations by starting with superposition state and comparing the phase shift introduced when letting the state evolve with and without an off resonant sechyp field present.

Off resonant excitation for the RF pulses

The maximum Rabi frequency of the RF pulses is approximately 50 kHz and therefore off resonant transitions should be negligible for these pulses. The closest level where the RF pulses could drive off resonant transitions is the aux-level 17 MHz below the ground level. For this level the maximum effect of off-resonant transitions is less than 0.3%.

6.1.4 Why single photon memories can't be simulated for AFC memories with spin wave storage

I found that the smaller population the data pulse transfers, the more sensitive the system becomes to the quality of the RF pulses. This is in fact quite obvious since a 0.1% fault on an RF pulse doubles the population in the spin level if initially 0.001 but makes a minor difference if initially 0.1. Thus you want the population in the spin state before the RF pulses to be much larger than the transfer rate of the RF pulses times the population in the ground state. The efficiency is in principle not affected by the increasing noise but the signal to noise ratio is raised the smaller the population that produces the echo. If the population in the spin state before the RF pulses is of the same order as the transfer rate of the RF pulses times the population in the ground state, the noise intensity will be of the same order as the echo intensity.

This will, however only be a problem in the simulations, not in the actual experiments. The reason for this is that the simulations are restricted to one spatial mode. This means that all noise will propagate in the same spatial direction. In the lab, however, the noise will be emitted in a random direction but the echo will only have a single spatial mode. Thus the actual signal to noise ratio will be much lower than in the simulations.

Assuming the detector to have an area of 5x5 mm^2 and be situated 1 m from the crystal, the experimental noise will be

$$\frac{25}{1000^2 \cdot 4\pi} \approx 2 \cdot 10^{-4}\%$$

of the noise level in the simulations.

In the simulations a pulse area of $\pi/15$ will be used. This pulse area is sufficiently big to give a good signal to noise ratio for the spin-wave storage simulations and sufficiently small so that the control pulses are not affected by unrealistic absorption effects. Since the intensity of the echo will scale with the intensity of the data-pulse, the efficiency will be independent of the pulse area of the data pulse and thus the results from these simulations can be used to draw conclusions about single photon storage efficiencies.

6.2 AFC with forward propagating echo

6.2.1 Simple AFC without control pulses

For comparison we will start to look at a simple AFC memory with echo in the forward direction. The theoretical estimations above imply that the efficiency of such a memory is limited to 54% and that the maximum echo is received at the effective absorption depth $\tilde{d} = 2$. In the figures 6.1-6.2 below a protocol with 10 AFC peaks with separation 1/2.7 MHz and finesse 6 was used. The AFC peaks were Super-Gaussian of order 10. The data pulse had frequency FWHM of 0.5 MHz. This gives an efficiency of 44.1%. Since the information will be coded in the phase of the field it is important to note that the phase is completely preserved in this process.

In figure 6.2 one can see the incoming data pulse at time zero and absorption depth zero. This pulse is then absorbed as it propagates through the crystal. 2.7 μs after the data pulse the ions are back in phase and an additional field starts to build up in the crystal. This is the echo pulse. The echo pulse has its maximum approximately at the effective absorption depth 2, which corresponds to a peak absorption depth of 12 for an AFC structure with finesse 6.

In figure 6.3 the intensity inside the crystal is shown for the peak absorption depths 0 and 12, respectively. Here, one can clearly see the incoming data pulse and the subsequent echo pulse.

Gaussian AFC-peaks

Except the fact that Super Gaussian AFC peaks give higher efficiencies it also simplifies the simulations since these peaks are easier to resolve, i.e. it demands less data points

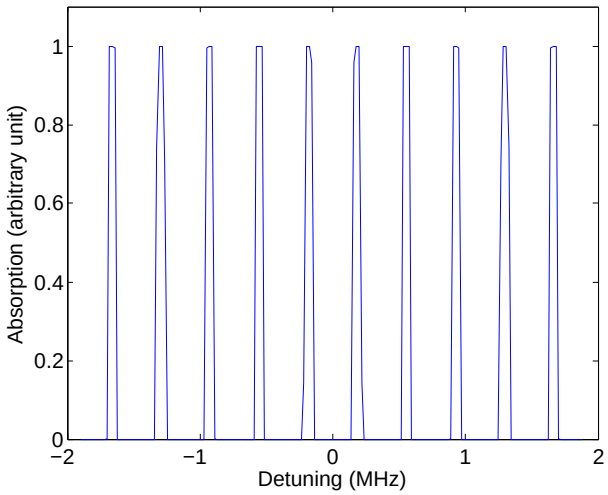

Figure 6.1: Super Gaussian absorption spectra used during AFC simulation.

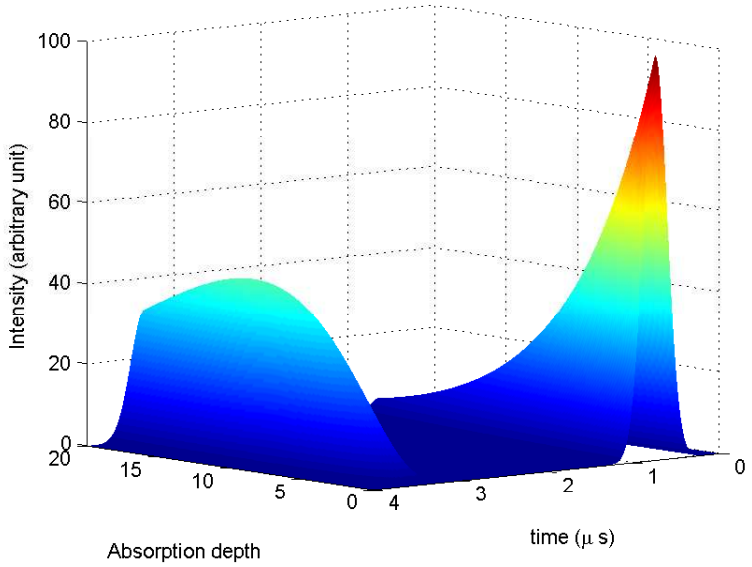

Figure 6.2: Data pulse and subsequent echo pulse for an AFC memory with 10 super Gaussian AFC peaks with separation 370 kHz and finesse 6. The data pulse had a pulse area of $\pi/15$. The efficiency is approximately 44%

in the detuning vector. However, experimentally these peaks are quite hard to achieve with the given finesse and peak spacing. It is thus also interesting to investigate the

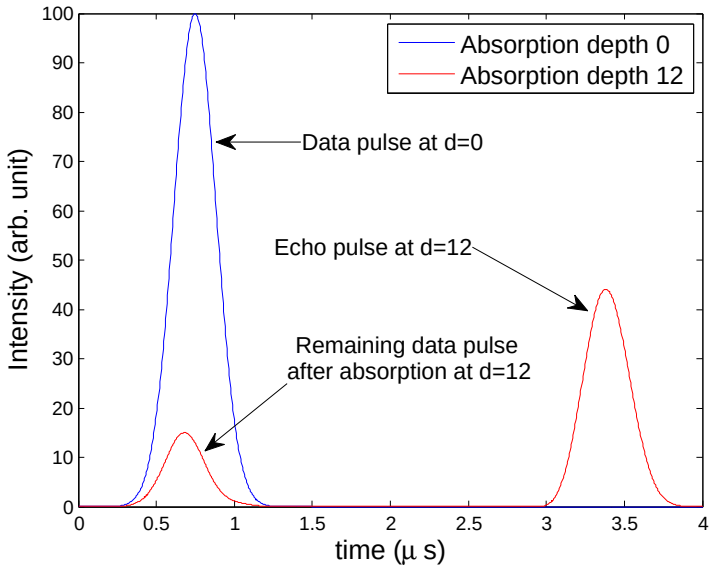

Figure 6.3: Intensity inside the material at the absorption depths 0 and 12, respectively. An AFC memory with 10 super Gaussian AFC peaks with separation 370 kHz and finesse 6 was used.

efficiency for Gaussian AFC-peaks. For Gaussian AFC-peaks the efficiency is reduced to 39.0% as can be seen in figures 6.4-6.5.

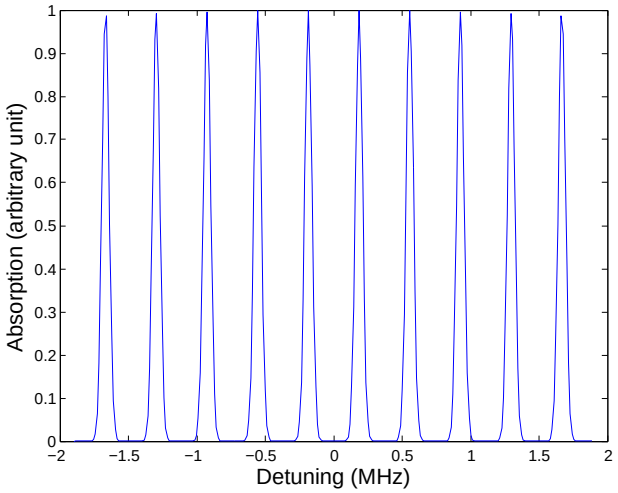

Figure 6.4: Gaussian absorption spectra used during AFC simulation.

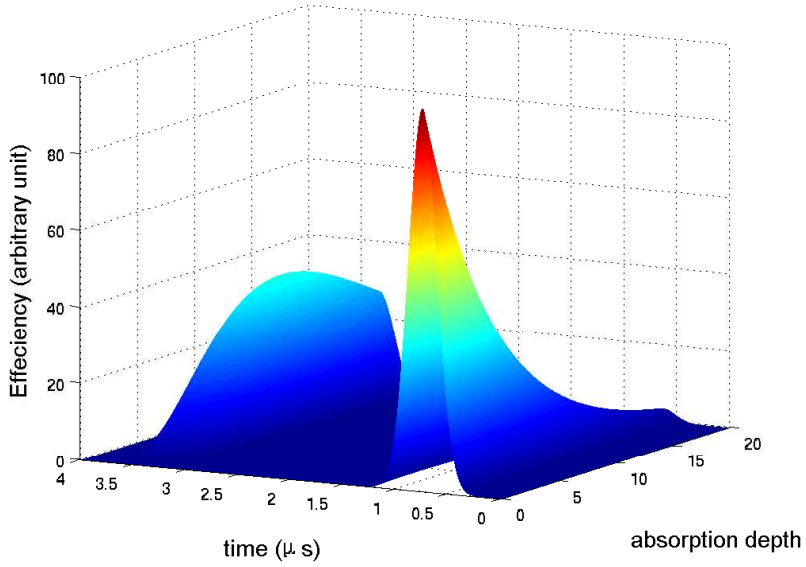

Figure 6.5: Data pulse and subsequent echo pulse for an AFC memory with 10 Gaussian AFC peaks with separation 370 kHz and finesse 6. The data pulse had a pulse area of $\pi/15$. The efficiency is approximately 39%

6.2.2 AFC with spin wave storage and RF-pulses

In the lab, the maximum possible Rabi-frequency of the RF-pulses is approximately 50kHz. This means that in order to achieve effective transfer one has to use sechyp pulses with amplitude FWHM of approximately 18 μs. Thus, the total duration of the pulse will be around 30-60μs. This is rather long compared with the natural time scale of the system and such simulations require very long computational times and huge memory capacities. However, if it is sufficient only to run Bloch simulations for the RF-pulses, omitting propagation effects, it is possible to reduce the computational time and memory requirement drastically. If the control pulses have high transfer rates the induced fields in the material will be small between the two control pulses. It thus seems reasonable that Bloch-simulations are sufficient between the first and the last control pulse, if the control pulses give sufficiently good transfer.

Assuming the control pulses to give >99% transfer ($c_3^2 \to 0.01c_3^2$) the coherences of the total density matrix for the 1-3 transition will be reduced to $1 - \sqrt{0.99} \approx 0.5\%$ of its original value. The total pulse area of the induced fields should roughly scale as the coherences and thus the induced fields will have pulse areas of 0.5% of the data pulse. If the data pulse has a pulse area of $\pi/15$ and duration 1μs, the maximum possible pulse area of the induced fields will be

$$\frac{\pi}{15} \cdot \frac{1}{200} = \frac{\pi}{3000}.$$

The effect of these fields on the echo should be negligible and thus it is sufficient to use Bloch simulations between the first and final control pulse.

Optimizing the control-pulses

In order to get high efficiencies the control pulses need to be thoroughly optimized. Due to the limited time between the data pulse and the echo pulse this proves to be a rather difficult task. To this end a two level Bloch Simulator written by Lars Rippe was used. The control pulses need to invert a total interval of approximately 3.4 MHz. However, since the frequency FWHM of the data pulse is as low as 0.5 MHz, the majority of the population is situated within an interval of 1 MHz. Thus it is important that the control pulses have extremely high transfer efficiency within this interval. The closest lying hyperfine level of the excited state is detuned 4.7 MHz relative to the level used in the experiments. Therefore it is also important that the population transfer to this level is small.

I found that sechscan pulses with high Rabi frequencies and a scan width of 1 MHz gave really good transfers even for cutoffs as short as 1 μs, see figure 6.6. For the simulations a maximum Rabi frequency of 2.3 MHz was chosen since this is in the vicinity of the maximum Rabi frequency possible to achieve in the lab.

In the upper five plots in figure 6.6 the population transfer for different detunings is shown. The different curves correspond to different choices of the maximum Rabi frequency, Ω_0. The centre frequency of the pulse is chosen as 0. From these plots one can see that the optimized pulse give a transfer rate of $> 99\%$ within a frequency interval of 2 MHz and $> 94\%$ within a frequency interval of 3 MHz. The two lower plots show the absolute value of the Rabi frequencies and the frequency chirps of the pulses.

Optimizing the RF-pulses

The spin level has a Gaussian broadening with a FWHM of 26kHz. The maximum Rabi frequency which is possible to achieve experimentally is 50 kHz. For these parameters I found that RF-pulses with a short scan and a cutoff of 67 μs gave a good transfer rate ($> 99\%$) over the entire inhomogeneous broadening of the spin state (see figure 6.7).

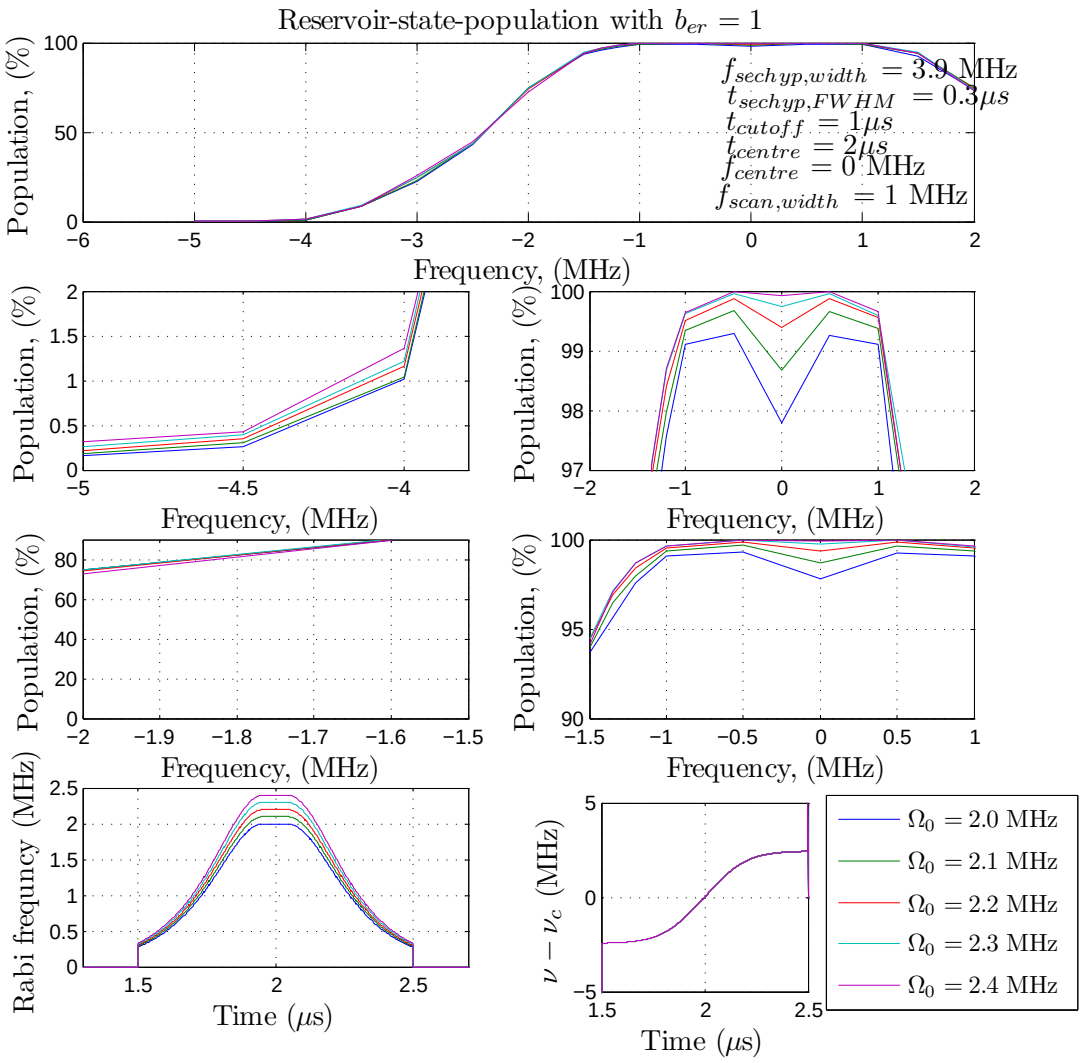

Figure 6.6: This figure shows population transfer, Rabi frequency and frequency chirp of sechscan pulses, used as control pulses, with different values of the maximum Rabi frequency. In the upper five plots the population transfer for different detunings is shown. The different curves correspond to different choices of the maximum Rabi frequency, Ω_0. The centre frequency of the pulse is chosen as 0. From these plots one can see that the optimized pulse gives a transfer rate of $> 99\%$ within a frequency interval of 2 MHz and $> 94\%$ within a frequency interval of 3 MHz. The two lower plots show the absolute value of the Rabi frequencies and the frequency chirps of the pulses. These plots were generated using a program written by L. Rippe.

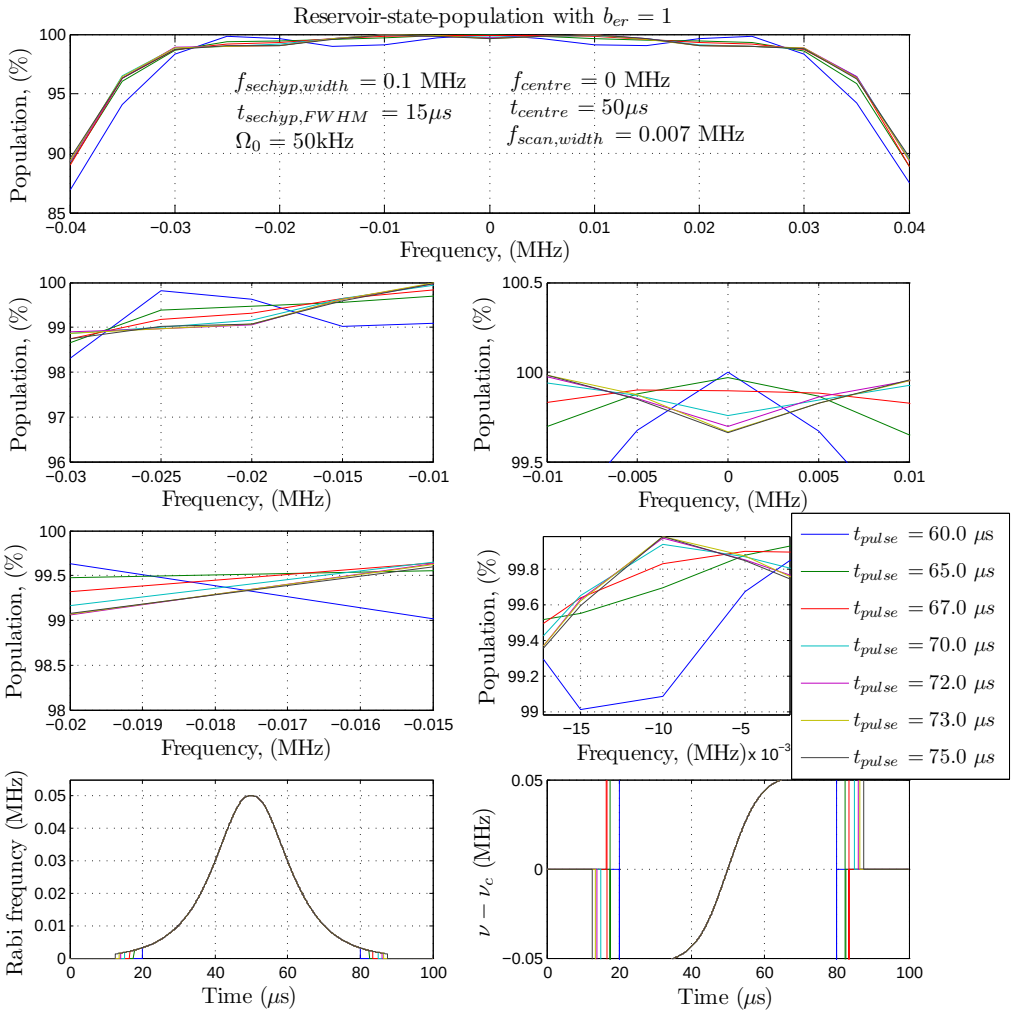

Figure 6.7: This figure shows population transfer, Rabi frequency and frequency chirp of the RF sechscan pulses with different cutoffs. In the upper five plots the population transfer for different detunings is shown. The different curves correspond to different choices of the cut-off time. The centre frequency of the pulse is chosen as 0. From these plots one can see that the pulse with a cutoff at 67 μs gives a transfer rate $> 99\%$ within an interval of 52kHz, which is twice the FWHM of the Gaussian inhomogeneous broadening of the spin state. The two lower plots show the absolute value of the Rabi frequencies and the frequency chirps of the pulses. These plots were generated using a program written by L. Rippe.

List of optimized pulses

Unless otherwise specified the optimized pulses in table 6.1 will be used.

Table 6.1: Optimized control and RF pulses. The parameters below are related to β and μ as follows: $\beta = 1.76/t_{FWHM,sechyp}$ and $\mu = (frequencywidth, sechyp) \cdot t_{FWHM,sechyp}/0.561$. The time of the frequency scan is given by $t_{scan} = 2\pi \cdot (scanwidth)/(\mu\beta^2)$

Pulse	frequency width, Sechyp	FWHM, sechyp	Ω_0	scan width	cutoff
control	3.9 MHz	0.3 μs	2.3 MHz	1 MHz	1 μs
RF	0.1 MHz	15 μs	50 kHz	7 kHz	67 μs

Are off-resonant effects a problem?

From the discussion in the last section we concluded that off-resonant effects could not be excluded for the control pulses and had to be investigated thoroughly. A first estimation of the effect of off-resonant excitation is obtained by looking at the relative phase-shift of different detunings with and without an off-resonant field present. The result of these calculations is shown in figure 6.8.

From a first glance on figure 6.8 one would expect off-resonant effects to be profound since it induces phase differences of the order of radians between the different frequency channels. However, that this is not the case can be seen from the following argument:

The AFC structure has a total width of about of 3.5 MHz. This would according to the data above give a maximum phase-shift of 0.5 radians. This phase shift corresponds to the phase shift that would be aquired from storing the state for

$$\frac{0.5}{26000 \cdot 2\pi} \approx 3\mu s$$

in the spin state.

From equation 5.11 we know that this would decrease the efficiency by a factor of

$$1 - e^{-2\cdot(26000\cdot 2\pi/4.7)^2\pi^2(3e-6)^2} \approx 0.5\%$$

which is quite small.

3-level simulations including off-resonant effects

Off-resonant effects can easily be included in the full model by adding a simultaneous off resonant field for the transition 1-3 during the control pulses between state 2 and 3. Performing simulations with the pulse sequences;

1. Data pulse. Gaussian with a frequency FWHM of 0.5 MHz and a time domain cutoff of 1.5 μs and t_0=0.75μs.

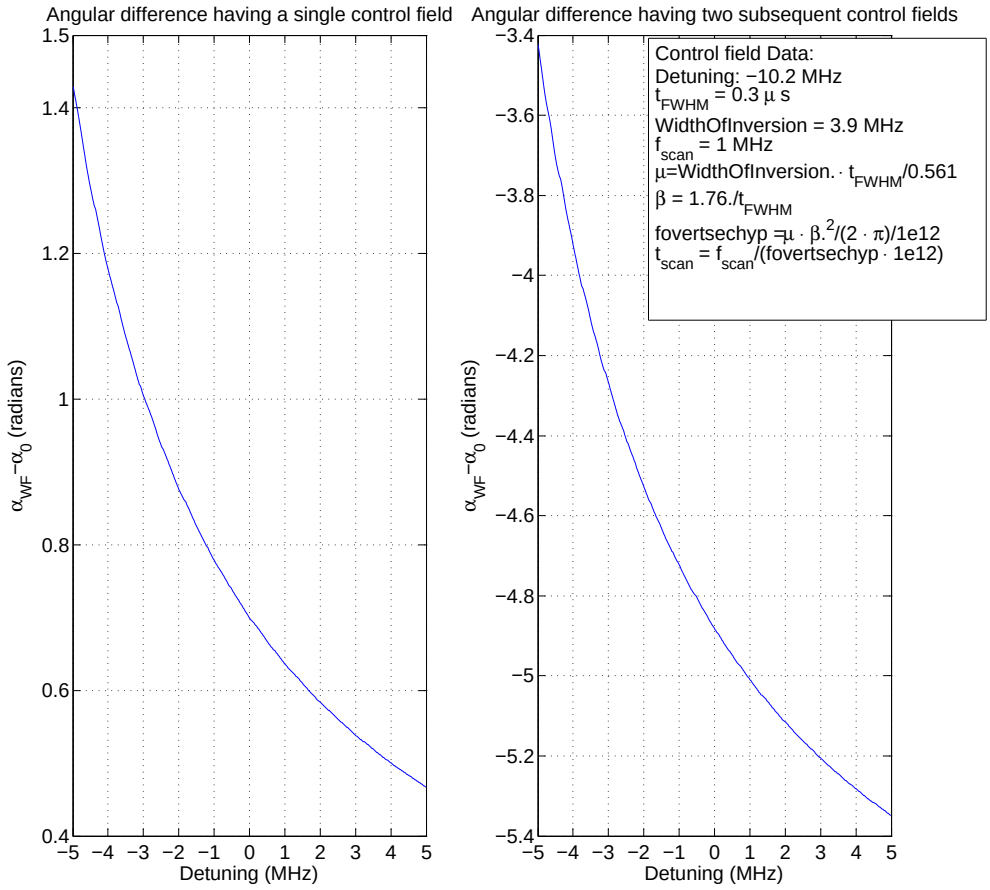

Figure 6.8: The relative phase-shift of different detunings with and without an off-resonant field present. The starting state was a 50-50 superposition between the ground state and the excited state. The optimized control pulse from table 6.1 with a detuning of -10.2 MHz relative to the zero-frequency was applied once (left) or twice (right). The graphs show a relative phase shift of approximately 0.5 radians between the different frequency channels of a 3.5 MHz broadened ensemble, after the two off resonant fields have been applied.

2. Control pulse. Optimized sechscan pulse at time t_0=2.5μs.

3. Control pulse. Optimized sechscan pulse at time t_0=3.5μs.

disregarding from the broadening of the spin state, the efficiency was 44.4% without off-resonant effects included and 43.3% with off-resonant effects included. Thus off-resonant transition effects introduced a decrease of only 1.1% of the efficiency. This result agrees

well with the qualitative argument above.

Another possible effect of off-resonant excitation could be that the phase of the echo-pulse is affected. In figure 6.9 the phase of the echo-pulse with and without off resonant effects included is shown. As before the spin state was not broadened in these simulations in order to isolate the effect of off resonant excitation.

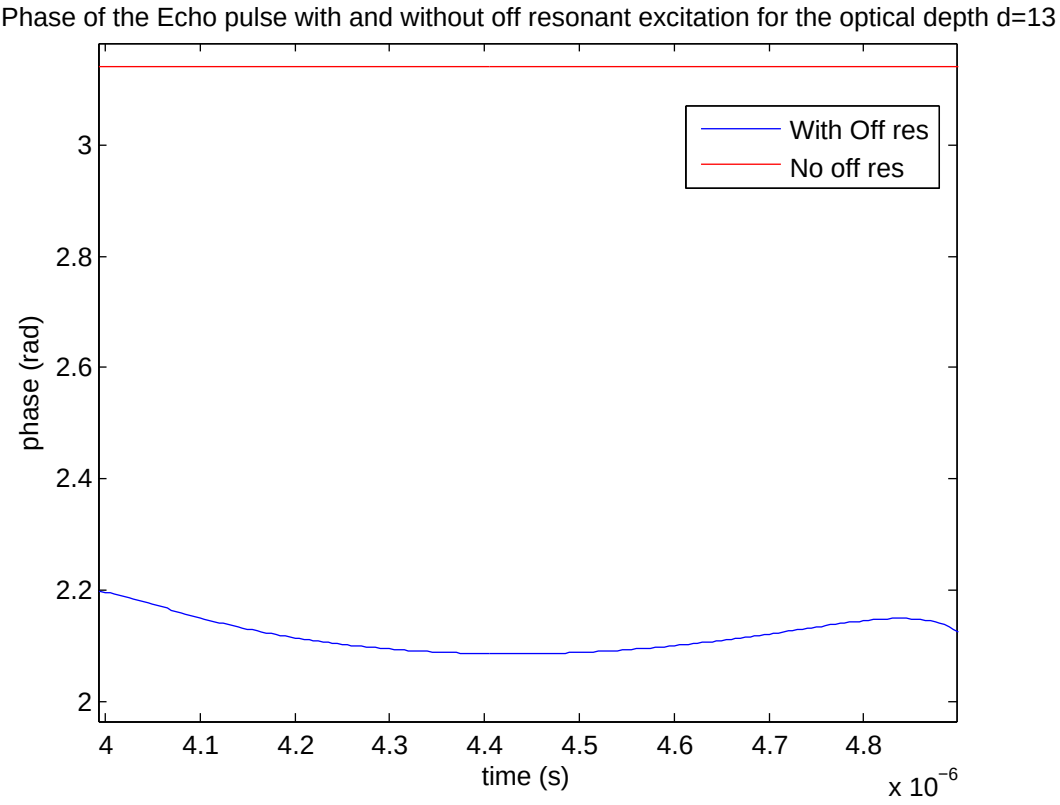

Figure 6.9: The phase of the echo-pulse with and without off resonant effects included. Two control pulses at times t_0=2.5μs and t_0=3.5μs were applied. The spin state was not broadened in these simulations in order to isolate the effect of off resonant excitation.

The constant phase shift of the echo pulse is not a problem since it will affect all modes in the same way and is easily compensated for. However, the phase fluctuations in time could become problematic. Although, in this case they are rather small for longer pulses the effects might be magnified.

6.2.3 Efficiency of AFC memory with spin-wave storage and forward propagating echo

In the table below the efficiency of a full quantum memory with spin wave storage, RF-pulses and super-Gaussian peaks is summarized. Simulations were performed for different coherence times of the spin level. In these calculations off-resonant effects were not included. By comparing row 1 and 3 in table 6.2 one can see that the efficiency loss due to the pulses are approximately 1.7%, which is really good. The remaining bottlenecks are thus the AFC structure and the coherence time of the spin-level. However, by making use of ZEFOZ techniques to increase the coherence time of the spin level (row 4 and 5) we can see that for storage 137.7 μs the coherence time of the spin level can be made sufficiently long.

As expected the efficiency is smaller for Gaussian AFC peaks than for super Gaussian peaks. The result of the calculations with Gaussian AFC peaks is shown in table 6.3.

Table 6.2: Efficiency for different AFC storage protocols with different life and coherence times, forward propagating echo and **Super-Gaussian** AFC peaks. Here Type is 1 for a simple AFC and 2 for AFC with spin wave storage. $T_{ij} = 1/\Gamma_{ij}$ and $T'_{ij} = 1/\Gamma'_{ij}$. The first two rows are the efficiencies for a simple AFC which can be used for comparison. Thus, the third row should be compared with the first row and the 4-6:th row with the second row. For AFC with spin wave storage the coherence times 500 μs, 10 ms and 800 ms have been chosen since it is the coherence time of the system without ZEFOZ techniques, and estimated coherence times that can be achieved with ZEFOZ techniques.

Type	Storage time	T_{12}	T_{13}	T_{23}	T'_{12}	T'_{13}	T'_{23}	Efficiency
1	2.7μs	∞	∞	∞	∞	∞	∞	46.5%
1	2.7μs	100s	273.5μs	431.8μs	500μs	100μs	100μs	44.1%
2	137.7μs	∞	∞	∞	∞	∞	∞	44.8%
2	137.7μs	100s	273.5μs	431.8μs	800ms	100μs	100μs	42.5%
2	137.7μs	100s	273.5μs	431.8μs	10ms	100μs	100μs	41.7%
2	137.7μs	100s	273.5μs	431.8μs	500μs	100μs	100μs	28.4%

Table 6.3: Efficiency for different AFC storage protocols with different life and coherence times, forward propagating echo and **Gaussian** AFC peaks. Here Type is 1 for a simple AFC and 2 for AFC with spin wave storage. $T_{ij} = 1/\Gamma_{ij}$ and $T'_{ij} = 1/\Gamma'_{ij}$. The first two rows are the efficiencies for a simple AFC which can be used for comparison. Thus, the third row should be compared with the first row and the 4-6:th row with the second row. For AFC with spin wave storage the coherence times 500 μs, 10 ms and 800 ms have been chosen since it is the coherence time of the system without ZEFOZ techniques, and estimated coherence times that can be achieved with ZEFOZ techniques.

Type	Storage time	T_{12}	T_{13}	T_{23}	T'_{12}	T'_{13}	T'_{23}	Efficiency
1	2.7μs	∞	∞	∞	∞	∞	∞	41.1%
1	2.7μs	100s	273.5μs	431.8μs	500μs	100μs	100μs	39.0%
2	137.7μs	∞	∞	∞	∞	∞	∞	40.6%
2	137.7μs	100s	273.5μs	431.8μs	800ms	100μs	100μs	38.5%
2	137.7μs	100s	273.5μs	431.8μs	10ms	100μs	100μs	37.7%
2	137.7μs	100s	273.5μs	431.8μs	500μs	100μs	100μs	25.7%

6.2.4 Effect of inhomogeneous RF -pulses

For large crystals the maximum Rabi frequency of the RF-pulse will vary throughout the crystal. Large crystals are essential in order to achieve high optical depths and therefore it is important to verify that the fluctuations in Rabi frequency don't affect the efficiency of the RF-pulses in a major way. From figure 6.6 we can see that the efficiency of sechscan pulses increase with increasing Rabi frequency. Thus, as long as the RF-pulses are optimized for the lowest Rabi frequency that will appear in the crystal the inhomogeneities should not be a problem. In order to verify this, simulations with a varying Rabi frequency

$$\Omega_{max}(z) = 1.3\Omega_0 exp(-\frac{ln(1.3)(z - z_{1/2})^2}{z_{1/2}^2}) \tag{6.2}$$

were performed. Here Ω_0 will be the minimum Rabi frequency which was set to 50kHz. The maximum Rabi frequency will be in the middle of the crystal and is chosen as $1.3\Omega_0$. For infinite life times and coherence times an efficiency of 44.4% was received for these RF-pulses. This can be compared with 44.8% which was received for homogeneous RF-pulses. Thus, the efficiency was reduced by a few tens of a percent. That the efficiency was reduced slightly can be understood from the fact the the RF-pulses were optimized for $\Omega_0 = 50kHz$. The oscillations in the transfer efficiency due to the square like behaviour near the pulse cutoff can then introduce a small decrease in the transfer efficiency.

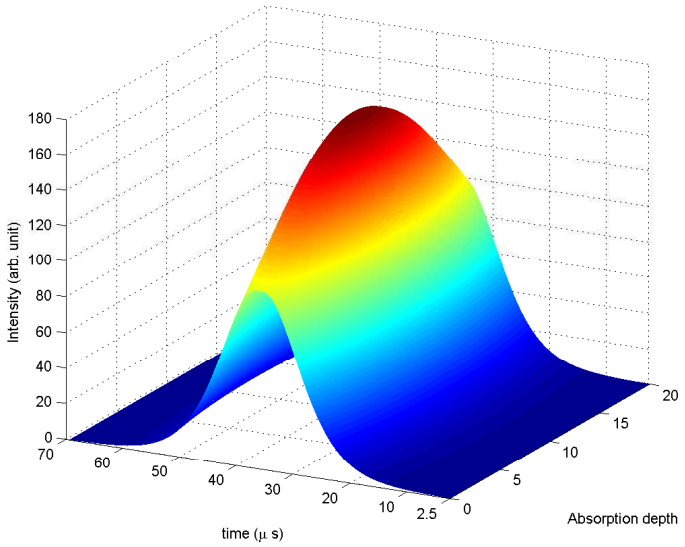

Figure 6.10: One of the RF-pulses used when investigating the effect of inhomogeneous RF-pulses on the efficiency of the AFC-protocol. The RF-pulse was the regular optimized RF-pulse from table 6.1, but the intensity of the pulse was varied like Gaussian function throughout the crystal.

6.3 AFC with backwards propagating echo

From figure 5.2 and equation 5.8 one can see that a backward propagating echo will increase the effeciency substantially. In order to incorporate a backwards propagating echo the loop over z was performed in the reverse direction during the last control pulse. For a simple AFC the simulation was simply stopped in the interval between the data pulse and the echo and the integration over z was reversed. This is rather unphysical since it is not possible to achieve AFC in the backwards direction without control pulses experimentally, but the result is important for comparison with the full simulations where control and RF pulses are included.

6.3.1 Simple AFC

A simple AFC with an absorption depth of 15 and finesse 6 should according to figure 5.2 give an efficiency slightly below 70%. In the simulations an efficiency of 69.5% was received with infinite life and coherence times and 65.9% with the actual life and coherence times of the system. The simulations were performed with an AFC structure consisting of 10 super Gaussian AFC peaks with peak separation 333 kHz and finesse 6.

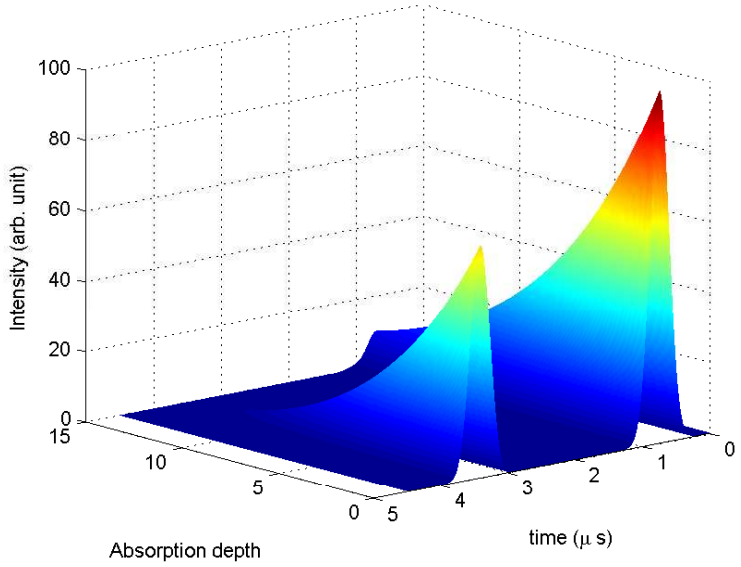

Figure 6.11: Data pulse and subsequent echo pulse in the backward direction for an AFC memory with 10 Super Gaussian AFC peaks with separation 333 kHz and finesse 6. The data pulse had a pulse area of $\pi/15$. The efficiency is approximately 44%

6.3.2 Gaussian Peaks

For Gaussian AFC peaks the efficiency was reduced to 65.2% with infinite life and coherence times and 61.8% with the actual life and coherence times of the system.

6.3.3 AFC with spin wave storage

A summary of the efficiencies for an AFC protocol with the optimized pulses, backwards propagating echo and different life and coherence times is given in table 6.4-6.5.

Table 6.4: Efficiency for different AFC storage protocols with different life and coherence times, backwards propagating echo and **super Gaussian** absorption peaks. The peak absorption depth was chosen to 15. Here Type is 1 for a simple AFC and 2 for AFC with spin wave storage. $T_{ij} = 1/\Gamma_{ij}$ and $T'_{ij} = 1/\Gamma'_{ij}$. The first two rows are the efficiencies for a simple AFC which can be used for comparison. Thus, the third row should be compared with the first row and the 4-6:th row with the second row. For AFC with spin wave storage the coherence times 500 μs, 10 ms and 800 ms have been chosen since it is the coherence time of the system without ZEFOZ techniques, and estimated coherence times that can be achieved with ZEFOZ techniques.

Type	Storage time	T_{12}	T_{13}	T_{23}	T'_{12}	T'_{13}	T'_{23}	Efficiency
1	2.7μs	∞	∞	∞	∞	∞	∞	69.5%
1	2.7μs	100s	273.5μs	431.8μs	500μs	100μs	100μs	65.9%
2	137.7μs	∞	∞	∞	∞	∞	∞	68.4%
2	137.7μs	100s	273.5μs	431.8μs	800ms	100μs	100μs	64.8%
2	137.7μs	100s	273.5μs	431.8μs	10ms	100μs	100μs	63.5%
2	137.7μs	100s	273.5μs	431.8μs	500μs	100μs	100μs	42.9%

Table 6.5: Efficiency for different AFC storage protocols with different life and coherence times, backward propagating echo and **Gaussian** AFC peaks. Here Type is 1 for a simple AFC and 2 for AFC with spin wave storage. $T_{ij} = 1/\Gamma_{ij}$ and $T'_{ij} = 1/\Gamma'_{ij}$. The first two rows are the efficiencies for a simple AFC which can be used for comparison. Thus, the third row should be compared with the first row and the 4-6:th row with the second row. For AFC with spin wave storage the coherence times 500 μs, 10 ms and 800 ms have been chosen since it is the coherence time of the system without ZEFOZ techniques, and estimated coherence times that can be achieved with ZEFOZ techniques.

Type	Storage time	T_{12}	T_{13}	T_{23}	T'_{12}	T'_{13}	T'_{23}	Efficiency
1	2.7μs	∞	∞	∞	∞	∞	∞	65.2%
1	2.7μs	100s	273.5μs	431.8μs	500μs	100μs	100μs	61.8%
2	137.7μs	∞	∞	∞	∞	∞	∞	64.3%
2	137.7μs	100s	273.5μs	431.8μs	800ms	100μs	100μs	60.9%
2	137.7μs	100s	273.5μs	431.8μs	10ms	100μs	100μs	60.0%
2	137.7μs	100s	273.5μs	431.8μs	500μs	100μs	100μs	40.3%

Chapter 7

Summary and conclusions

In this work a program for simulating three-level optical quantum memories was developed. The program was used to investigate AFC-memories but it can easily be generalized so that also CRIB and GEM memories[1] can be simulated. Control pulses and RF-pulses for the AFC-memory were developed and the efficiency of an AFC scheme with these pulses was calculated by making use of the three-level simulator.

From the result presented in the last section we can see that, with the current technology, efficiencies up to 38.5% are possible to achieve with forward propagating echo and up to 60.9% with backward propagating echo, for Pr-doped Yttrium silicate based AFC memories with spin state storage. Off-resonant excitation during the control pulses as well as inhomogeneous RF-fields can introduce a small decrease in the efficiency but this effect should still be less than 2%. The main bottle-necks for achieving higher efficiencies is the finesse and peak type of the AFC-structure. From the result presented in the last section we can see that the efficiency can be raised with a few per cent if super Gaussian peaks are used. However, to reach efficiencies higher than 90% the finesse of the AFC-structure need to be increased. The reason for the low finesse used in these simulations is that the peak spacing needs to be small in order to give sufficient time for the control pulses to transfer the population from the excited to the spin state. For the current technology the finesse is then limited to approximately 6 for the given peak spacing. However, by changing material from Pr to Eu based memories the quantum information group in Lund expects that the finesse could be increased substantially for the given peak spacing and thus higher efficiencies can be achieved. Another way of increasing the finesse would be to increase the Rabi-frequency of the control pulses. With higher Rabi-frequencies the same transfer efficiencies can be reached for shorter pulses. And thus this would allow for larger peak separations. However, higher Rabi-frequencies would also increase off resonant excitation effects.

When investigating off-resonant excitation effects we saw that both the efficiency and

[1]These are other types of optical quantum memories where the rephasing process is induced by the use of external electric fields.

also the phase of the echo was affected. The effect on the phase could be divided into two parts. One (in time) constant offset and one phase-shift which varied in time. The constant phase-shift should affect all modes equally and if not, is easy to compensate for. However the varying phase shift could be a bigger problem. That this phase modulation occurs can be understood from the fact that off resonant excitation affects the different frequency channels of the ensemble differently and thus also the phase of the different Fourier modes of the echo-pulse. For the parameters used in this simulation this phase-shift was quite small. However, under different circumstances the shift could be bigger. What is important to take with us from this work is that such phase modulations could depend on off-resonant excitation effects and can in that case be reduced by reducing the Rabi-frequency of the control pulses.

The storage time is mainly limited by the coherence time of the ground state hyperfine levels. And thus, longer storage times can be achieved by increasing the coherence time of the spin level in the current material or use other materials such as Europium with longer coherence times.

The main obstacle with the simulations was that the full simulations requires long computational times and huge memory capacities. This was solved by dividing the simulations so that the spatial dependence of the fields was ignored during the RF-pulses. However, still full simulations require at least 4 hours and often up to 15 hours of computational time. The long computational times could be reduced by rewriting the program in another language. Previous Maxwell-Bloch simulations have shown that rewriting the programs from Matlab to C++ could reduce the computational time by approximately a factor 0.5 [11]. However, to be able to perform full simulations multiple computers should be used. This can be done either with computer clusters which would give more threads to run the single simulations on, or by just making use of many computers and run many different simulations simultaneously.

7.1 Acknowledgements

I would like to thank Lars Rippe and Stefan Kröll for their help and support during this project. I would also like to thank the entire quantum information group for the enlightening discussions and nice company during my time with them.

Bibliography

[1] P. W. Shor, "Polynomial-time algorithms for prime factorization and discrete logarithms on a quantum computer," *Siam J. Sci. Statist. Comput.*, vol. 26, p. 1484, 1997.

[2] N. Gisin, G. Ribordy, W. Tittel, and H. Zbinden, "Quantum cryptography," *Reviews of Modern Physics*, vol. 74, p. 144, 2002.

[3] H. Hubel, M. R. Vanner, T. Lederer, B. Blauensteiner, *et al.*, "High-fidelity transmission of polarization encoded qubits from an entangled source over 100 km of fiber," *Optics Express*, vol. 15, pp. 7853–7862, June 2007.

[4] W. Tittel, B. Brendel, B. Gisin, T. Herzog, *et al.*, "Experimental demonstration of quantum correlations over more than 10 km," *Phys. Rev. A*, vol. 57, pp. 3229–3232, 1998.

[5] E. Schillinger, "Money changes hands in key bank transactions," *Nature*, vol. 428, p. 883, Apr. 2004.

[6] W. K. Wootters and W. H. Zurek, "A single quantum cannot be cloned," *Nature*, vol. 299, pp. 802–803, 1982.

[7] H.-J. Briegel, W. Dur, J. I. Cirac, and P. Zoller, "Quantum repeaters for communication," 1998. http://arxiv.org/abs/quant-ph/9803056.

[8] M. Afzelius, C. Simon, H. de Riedmatten, and B. Gisin, "Multimode quantum memory based on atomic frequency combs," *Physical Review A*, vol. 79, p. 52329, 2009.

[9] H. de Riedmatten, M. Afzelius, M. Staudt, C. Simon, and N. Gisin, "A solid state light-matter interface at the single photon level," *Nature*, vol. 456, p. 773, 2008.

[10] M. Sabooni, M. Huang, S. Kröll, M. Afzelius, *et al.*, "Towards an efficient atomic frequency comb quantum memory," *Journal of Luminescence*, vol. 130, 2010.

[11] A. Thuresson, "Numerical simulations of highly efficient quantum memories," Master's thesis, Lund University, 2011. LRAP-439.

[12] M. A. Nielsen and I. L. Chuang, *Quantum Computation and Quantum Information.* Cambridge University Press, 10 ed., 2010.

[13] J. Sakurai, *Modern Quantum Mechanics, Revised Edition.* Addison-Wesley, 1994.

[14] D. Styer, M. Balkin, K. Becker, T. Wotherspoon, S. Forth, M. Kramer, D. Oertel, and M. Rinkoski, "Nine formulations of quantum mechanics," *Am. J. Phys.*, vol. 70, pp. 288–297, March 2002.

[15] G. T. Purves, *Absorption and dispersion in atomic vapours: applications to interferometry.* PhD thesis, University of Durham, 2006.

[16] Y. B. Band, *Light and matter: electromagnetism, optics, spectroscopy and lasers.* Wiley, 2006.

[17] C. Foot, *Atomic Physics.* Oxford University Press, 2005.

[18] J. Jackson, *Classical Electrodynamics 3:th edition.* Wiley, 1999.

[19] L. Mandel and E. Wolf, *Optical coherence in quantum optics.* Cambridge University Press, 1995.

[20] M. Nilsson, *Coherent Interactions in Rare-Earth-Ion-Doped Crystals for Applications in Quantum Informations Science.* PhD thesis, Lund Institute of Technology, 2004. LRAP-333.

[21] R. H. Dicke, "Coherence in spontanious radiation processes," *Physical Review*, vol. 93, 1954.

[22] N. Sangouard, C. Simon, M. Afzelius, and B. Gisin, "Analysis of a quantum memory for photons based on controlled reversible inhomogeneous broadeningsan," *Physical Review A*, vol. 75, p. 32327, 2007.

[23] S. A. Moiseev and S. Kröll, "Complete reconstruction of the quantum state of a single-photon wave packet," *Phys. Rev. Lett.*, vol. 87, p. 173601, 2001.

[24] E. Fraval, M. J. Sellars, and J. J. Longdell, "Method of extending hyperfine coherence times in Pr^{3+}:Y_2SiO_5," *Phys. Rev. Lett.*, vol. 92, p. 077601, Feb 2004.

[25] E. Fraval, M. J. Sellars, and J. J. Longdell, "Dynamic decoherence control of a solid-state nuclear-quadrupole qubit," *Phys. Rev. Lett.*, vol. 95, p. 030506, Jul 2005.

[26] M. Lovric, P. Glasenapp, D. Suter, B. Tumino, A. Ferrier, P. Goldner, M. Sabooni, L. Rippe, and S. Kröll, "Hyperfine characterization and spin coherence lifetime extension in Pr^{3+}:$La_2(WO_4)_3$," *Phys. Rev. B*, vol. 84, p. 104417, Sep 2011.

[27] M. Afzelius and C. Simon, "Impedance-matched cavity quantum memory," *Physical Review A*, vol. 82, p. 22310, 2010.

[28] S. A. Moiseev, S. N. Andrianov, and F. F. Gubaidullin, "Efficient multimode quantum memory based on photon echo in an optimal qed cavity," *Phys. Rev. A*, vol. 82, p. 022311, 2010.

[29] S. T. Kometa, "Quantum state storage in rare-earth doped crystal placed inside a cavity," Master's thesis, Lund University, 2011. LRAP-437.

[30] L. Rippe, *Quantum Computing with Naturally Trapped Sub-Nanometre-Spaced-Ions*. PhD thesis, Faculty of Engineering LTH, Lund University, 2006. LRAP-365.

[31] M. S. Silver, R. I. Joseph, and D. I. Holt, "Selective spin inversion in nuclear-magnetic resonance and coherent optics through an exact solution of the bloch riccati equation," *Phys. Rev. A*, vol. 31, pp. R2753–R2755, 1985.

[32] M. Bonarota, J. Ruggiero, J. L. L. Gouët, and T. Chanelière, "Efficiency optimization for atomic frequency comb storage," *Phys. Rev. A*, vol. 81, p. 033803, Mar 2010.

[33] D. Kiryanov and E. Kiryanova, *Computational Science*. Infinity Science Press, 2007.

Appendix A

Documentation of the program

In this chapter I give a short documentation of the three-level Maxwell Bloch simulator developed in this project. The program was written in MATLAB and consists of three main parts;

1. Input creator
2. Maxwell Bloch Solver
3. Bloch Solver

Each of these main parts then makes use of a variety of subroutines.

A.1 Input creator

The input creator creates a binary input file, input.mat, which is loaded by the two solvers. In this file the pulse sequences, material properties and output files are defined.

A.2 Maxwell-Bloch Solver

The Maxwell-Bloch solver loads the input file created by the input creator. It defines the initial density matrix. There are three options for the initial density matrix: either all ions can start in one of the two hyperfine ground states ($|g\rangle$ and $|s\rangle$), or the solver can load the resulting density matrices from a previous run which should be stored in variables n1IN, n2IN, rho12IN etc and saved in binary files with the same name. Which of these options that are chosen is governed by the value of the variable 'initial_state' defined in the input creator.

The output of the MB-solver is the intensity of the fields (Int13, Int23), the off-diagonal elements of the Hamiltonian (Hoff, corresponding to the amplitude of the fields) the integrated density matrix (rho) and if 'save_state' is set to 1, also the final density matrix for all detunings and spatial positions (n1OUT, n2OUT, rho12OUT etc). Hoff can be used to extract the phase of the field by using the program PlotPhase.

A.3 Bloch-Solver

The Bloch-solver works in the same way as the MB-solver only that here the spatial dependence of the electric and magnetic fields is ignored.

A.4 List of subroutines

- createAFC
- dRho
- GaussPulse
- GaussPulse_trunc
- GaussPulse_truncA
- RKbloch
- sech_pulse
- sech_pulse_truncated
- smoothsecscan (written by L. Rippe)
- smoothsecscan_parameters (written by L. Rippe)
- sq_pi

A.5 Example of script

For long runs it is convenient to write a script where the different programs are called. The idea is that you have a number of input creators that define the crystal and the pulse sequences for that particular run. E.g. in the first input creator you would typically define the data pulse and first control pulse, in the second input creator you would define the first RF-pulse, in the third input creator you would define the second RF-pulse and in the fourth input creator the second control pulse. These input creators are then called from a script.

A.5.1 Example of script for forward propagating echo

Below follows an example of a script for a forward propagating echo:

```
clear all
close all
```

```
%*****DATA PULSE AND FIRST CONTROL PULSE*****%
create_input1          %input creator for data pulse and first control pulse
pause(5)
MaxBlochMain           %starting maxwell bloch simulations. The input file ...
                       %created by create_input1.m will be used

%save integrated density matrix and intensities from first simulation
disp('First MB simulation finished')
save('50usGAMMA0/rhoA.mat','rho')
save('50usGAMMA0/Int13A.mat','Int13')
save('50usGAMMA0/Int23A.mat','Int23')

%save for input for next run
n1IN=n1OUT;
n2IN=n2OUT;
rho12IN=rho12OUT;
rho13IN=rho13OUT;
rho23IN=rho23OUT;
save('n1IN.mat','n1IN')
save('n2IN.mat','n2IN')
save('rho12IN.mat','rho12IN')
save('rho13IN.mat','rho13IN')
save('rho23IN.mat','rho23IN')
pause(5)


%*****FIRST RF PULSE*****%
create_inputRF %input creator for first RF pulse
pause(5)
BlochMain      %Starting Bloch simulation for first RF pulse

disp('First Bloch simulation finished')
save('50usGAMMA0/rhoRF1.mat','rho') %save integrated density matrix for
                                    %simulation


%save for input to next run
n1IN=n1OUT;
n2IN=n2OUT;
rho12IN=rho12OUT;
rho13IN=rho13OUT;
rho23IN=rho23OUT;
```

```
save('n1IN.mat','n1IN')
save('n2IN.mat','n2IN')
save('rho12IN.mat','rho12IN')
save('rho13IN.mat','rho13IN')
save('rho23IN.mat','rho23IN')
pause(5)

%*****SECOND RF PULSE*****%
create_inputRF %in this case two identical RF-pulses were used, thus the
               %same input creator is used as in the previous run
pause(5)
BlochMain      %Starting Bloch simulation for second RF pulse

disp('Second Bloch simulation finished')

save('50usGAMMA0/rhoRF2.mat','rho') %save integrated density matrix for
                                    %simulation

%save for input to next run
n1IN=n1OUT;
n2IN=n2OUT;
rho12IN=rho12OUT;
rho13IN=rho13OUT;
rho23IN=rho23OUT;

save('n1IN.mat','n1IN')
save('n2IN.mat','n2IN')
save('rho12IN.mat','rho12IN')
save('rho13IN.mat','rho13IN')
save('rho23IN.mat','rho23IN')
pause(5)


%*****SECOND CONTROL PULSE*****%
create_input2       %input creator for second control pulse

MaxBlochMain        %starting Maxwell Bloch simulation

%Save result in binary files
save('50usGAMMA0/rhoB.mat','rho')       %integrated density matrix
save('50usGAMMA0/Int13B.mat','Int13')   %Intensity of 13-field
save('50usGAMMA0/Int23B.mat','Int23')   %Intensity of 23-field
```

```
save('50usGAMMA0/Hoff.mat','Hoff')      %Off-diagonal matrix elements of
                                        %the Hamiltonian
save('50usGAMMA0/zgrid','zgrid')        %z-grid for plot
save('50usGAMMA0/tgrid.mat','tgrid')    %t-grid for plot

disp('SIMULATION FINISHED')
```

A.5.2 Example of script for backward propagating echo

In chapter 5 it was mentioned that in order to simulate a backward propagating echo the order of the loop over z was reversed for the last control pulse. In the simulations this was achieved by flipping the initial density matrix in the dimension corresponding to the z direction and performing the loop in the forward direction. When the simulation is finished all data matrices containing the result needs to be flipped back. Below follows an example of the part of the script corresponding to the second RF-pulse and last control pulse.

```
%***THIS IS NOT THE ENTIRE SCRIPT!****%

%*****SECOND RF PULSE*****%
create_inputRF %in this case two identical RF-pulses were used, thus the
               %same input creator is used as in the previous run
pause(5)
BlochMain      %Starting Bloch simulation for second RF pulse

disp('Second Bloch simulation finished')

save('50usGAMMA0/rhoRF2.mat','rho') %save integrated density matrix for
                                    %simulation

%save for input to next run. Order of z is reversed.
n1IN=flipdim(n1OUT,3);
n2IN=flipdim(n2OUT,3);
rho12IN=flipdim(rho12OUT,3);
rho13IN=flipdim(rho13OUT,3);
rho23IN=flipdim(rho23OUT,3);

save('n1IN.mat','n1IN')
save('n2IN.mat','n2IN')
save('rho12IN.mat','rho12IN')
save('rho13IN.mat','rho13IN')
save('rho23IN.mat','rho23IN')
pause(5)
```

```
%*****SECOND CONTROL PULSE*****%
create_input2          %input creator for second control pulse

MaxBlochMain           %starting Maxwell Bloch simulation

%restoring order of z
Int13=flipdim(Int13,2); %z is the second dimension
Int23=flipdim(Int23,2);
Hoff=flipdim(Hoff,3); %Here z is the third dimension

%Save result in binary files
save('50usGAMMA0/rhoB.mat','rho')          %integrated density matrix
save('50usGAMMA0/Int13B.mat','Int13')      %Intensity of 13-field
save('50usGAMMA0/Int23B.mat','Int23')      %Intensity of 23-field
save('50usGAMMA0/Hoff.mat','Hoff')         %Off-diagonal matrix elements of
                                           %the Hamiltonian
save('50usGAMMA0/zgrid','zgrid')           %z-grid for plot
save('50usGAMMA0/tgrid.mat','tgrid')       %t-grid for plot

disp('SIMULATION FINISHED')
```